Columbia University in the City of New York | New York, N.Y. 10027
OFFICE OF PROJECTS AND GRANTS
BOX 20, LOW MEMORIAL LIBRARY

NASA Cooperative Agreement NCC 5-29

Semi-Annual Progress Report

April 1990 - September 1990

Semi-Annual Progress Report for the period 4/1/90-9/30/90

TASK A: CLIMATE AND ATMOSPHERIC MODELING STUDIES

Climate Model Development and Applications

The research conducted during the past year in the climate and atmospheric modeling programs has concentrated on the development of appropriate atmospheric and upper ocean models, and preliminary applications of these models. Principal models are a one-dimensional radiative-convective model, a three-dimensional global climate model, and an upper ocean model. Principal applications have been the study of the impact of CO_2, aerosols and the solar 'constant' on climate.

Progress has been made in the 3-D model development towards physically realistic treatment of these processes. In particular, a map of soil classifications on $1^{\circ} \times 1^{\circ}$ resolution has now been digitized, and soil properties have been assigned to each soil type. Using this information about soil properties, a method has been developed to simulate the hydraulic behavior of soils of the world. This improved treatment of soil hydrology, together with the seasonally varying vegetation cover, will provide a more realistic study of the role of the terrestrial biota in climate change.

A new version of the climate model has been created which follows the isotopes of water and sources of water (or colored water) throughout the planet. Each isotope or colored water source is a fraction of the climate model's water. It participates in condensation and surface evaporation at different fractionation rates and is transported by the dynamics. A major benefit of this project has been to improve the programming techniques and

physical simulation of the water vapor budget of the climate model. Applications include simulations of deuterium and oxygen-18 for both current climate and 18,000 years ago, the source of precipitation in each grid box in the North Hemisphere, and a stratospheric tritium experiment to simulate the atomic testing of the 1950s and 60s (Koster et al., 1990).

During the past year, papers have been published, which investigate the ability of the climate model to initiate ice ages (Rind et al., 1989), and the likelihood of future drought caused by the projected increase in temperatures (Rind et al., 1990).

Work supervised by Dr. Jonathan T. Overpeck has concentrated on two main fronts during 1989-1990: 1) modeling of the interaction between climate and vegetation, past, present, and future, and 2) a model-based assessment of past climatic change, particularly over the last deglaciation and during the Little Ice Age. The purpose of this work has been to develop and test the same vegetation and climate models that are used to simulate future environmental change.

During this last research period, two vegetation modeling projects have been completed and the results published. The first project used statistical and process-oriented models to simulate the climate-induced vegetation change that took place over the last glacial to interglacial transition (18,000 yr. B.P. to present). GCM simulations of past climate (NCAR and GISS) were input into the vegetation models and the resulting simulated vegetation change was compared to that reconstructed using a network of over 250 radiocarbon-dated pollen records from eastern North America. The conclusion of thse comparisons (Overpeck and Bartlein, 1989 and Overpeck et al., 1990a) suggests that the use of state-of-the-art models

can yield realistic simulations at the sub-continental scale. The next step of the investigation, also published in these two papers, was to apply the same models to simulate the equilibrium climatic change that could occur over the next 200 years in response to increased atmospheric greenhouse gas concentrations. These results, backed up by the paleoclimate/vegetation model validation, suggest strongly that future change may be unprecedented, both in size and rate. The results were used in EPA Report to Congress (1989) and were the first of their kind where extensive validation was included.

Although the first component of the vegetation modeling focused on the equilibrium pattern of climatic change, sensitivity studies were also conducted to determine how fast future change may occur. The work was carried out with a forest stand simulation model and highlighted the importance of changing climatic variability and forest disturbance in altering the composition and biomass of natural forests. Results suggest that significant climate-induced change may be detectable as early as the first quarter of the next century (Overpeck et al., 1990b). Colin Price (GRA Columbia) has begun to quantify the effects of climate change on vegetation.

The vegetation modeling effort has now shifted to the reconstruction and modeling of vegetation change at low latitudes, primarily Africa. This effort, being carried out in collaboration with French scientists, will allow us to test how well tropical climate especially the hydrologic cycle and vegetation can be simulated. A new database of climate and vegetation change for Africa spanning the past 30,000 years has been established and new vegetation modeling procedures are being developed for simulating

changes in the distribution of vegetation regions. The modeling procedure has advantages over existing vegetation-climate classification schemes (e.g. Holdridge), in that it uses statistical methods to fit the form of the non-linear climate-vegetation relationship and because it allows estimation of the probabilities of occurrence for multiple different vegetation types in a given grid box.

Modeling of the climate and vegetation change of the last 30,000 years, and of the Little Ice Age, has begun with the hiring of Rick Healy and initial attempts to compile appropriate boundary conditions for GCM runs.

This past year, Atlantic coastal paleoclimatic studies, which have generated new data, have focused on studies of the last deglaciation, from about 18,000 yr BP, to the beginning of the Holocene warming at 10,000 yr BP. Analysis of three northeastern late-glacial sites have been completed, and the pollen and macrofossil record at Alpine Swamp, New Jersey, together with accelerator mass spectrometry C-14 dating, was recently published (Peteet et al., 1990).

North Pacific coastal studies continued with the discovery of a 23,000 yr BP peat layer from Kodiak Island, which confirmed the existence of an ice-free environment during global full-glacial conditions. Pollen analysis of the deglaciation on Kodiak Island is in progress. A paper concerning the glacial-interglacial migratory history of lodgepole pine and the associated climate change in southern Alaska was recently submitted (Peteet, 1990). A paper documenting the ages of a volcanic eruption in southeastern Alaska has also been submitted (Reihle et al., 1990).

The southeastern U.S. field initiative for a transect of pollen cores from Virginia south to Georgia was completed with the acquisition of four cores. Margaret Kneller, a Columbia University GRA, has finished processing one of the cores and is currently analyzing pollen and macrofossils (Kneller and Peteet, 1990).

A paper comparing the timing of Milankovitch forcing and paleoclimatic data from ocean, land, and ice has been accepted (Peteet et al., 1990).

The computer code of the ocean general circulation model has been streamlined so that different numerical treatments can be implemented and tested. The streamlined code has been verified against the simulations of Cox (1984).

Progress has been made in implementing several vertical differencing schemes in the model, which include second and fourth order schemes. Sensitivity experiments are ongoing to test the effects of these schemes.

A necessary step in using ocean color data to understand the ocean's role in the global carbon cycle is the derivation of incident solar radiation at the surface, as a forcing term for marine productivity. A computationally-efficient scheme for deriving surface solar radiation has been developed. The scheme incorporates 3-hourly data on cloud properties derived from the International Satellite Cloud Climatology Project. Comparison with ground truth shows that the scheme is accurate to $\pm$ 7 w/m^2.

A global coastal hazards data base is being compiled to identify shorelines at high risk to anticipated future sea level rise, caused by greenhouse-gas-induced climate warming. Data has been compiled for seven coastal variables, from various sources, for the entire U.S., and the data base is currently being extended to Canada and Mexico (Gornitz, 1990b).

Each of the variables, relating to inundation and erosion risks, is assigned a rank from 1 to 5, based on assessment of the relative risk factor. These risk factors are then combined into an overall coastal vulnerability index, CVI. Experimentation with various forms of CVI and weighting factors is in progress.

Results for the East Coast, U.S.A., as a test case, indicate a region of relatively high vulnerability. For example, 61% of the land near the shoreline lies at an average elevation of 5 m or less, around 3/4 of coastal materials consists of unconsolidated sediments, and dominant landforms include estuaries (42% by length), barrier coasts (18%) and lagoons (15%), with rocky, embayed coasts (12%), concentrated in New England. Furthermore, 89% of the region is subsiding at rates exceeding 2 mm/yr, or 1.5 - 2 times the global eustatic range of 1-2 mm/yr. A quarter of the coast is eroding at rates greater than 1 m/yr, while around 2/3 experiences shoreline displacements within ± 1 m/yr (Gornitz, 1990c).

High risk areas along the East Coast have been identified along parts of Cape Cod, Long Island and the New Jersey barrier beaches, the North Carolina Outer Banks, the southern Delmarva Peninsula, and the Georgia-South Carolina. Other high risk regions include the Louisiana-Texas coast and the Sacramento-San Joaquin Delta, California.

SAGE II

In accordance with the task to carry out modeling and interpretation of SAGE II data, a 23-level version of the 3-D GCM to be used has been developed. This model extends from the surface up to 0.01 mb (≈85 km). Model improvements during the past year include the incorporation of gravity wave-induced stratospheric drag. With the incorporation of parameterization

for model generated gravity waves from the sources of topography, wind shear and convection, realistic simulations of the middle atmospheric climatology have been made. An analysis of the SAGE retrieval of water vapor in the tropical lower stratosphere has been investigated.

A paper has been recently published, which investigates the impact of doubled CO_2 on the climate of the stratosphere (Rind et al., 1990).

TASK B: CLIMATE APPLICATIONS OF EARTH AND PLANETARY OBSERVATIONS

Cloud Climatology

Over the past year, the statistical study, completed last year, has been extended to the remainder of the globe, and to all seasons (paper in preparation). Basic findings confirm the more limited results, but show that the increase in land surface temperature variability in winter is generally not as large as expected. Instead, the passage of synoptical fronts is associated with large temperature changes, but over a small time period and surface area. Thus, in contrast to summer conditions, the "average" winter variability is similar to that in summer, but with infrequent, larger changes. This result suggests that significant improvement in cloud detection algorithms could be made by including synoptic weather reports as an auxiliary data set. Therefore the time record analysis in the algorithm will "know" where to place a boundary between two time periods with different characteristics. The first extension of these results to the remaining spectral channels of AVHRR is also underway, using the ISCCP cloud detection analysis results.

The initial technique for identifying tropical convective cloudiness showed the presence of two characteristic cloud types: one associated with deep convective towers and the other associated with mesoscale anvil and cirrus clouds. Comparisons with surface-based precipitation measurements indicated that, to explain the phase of diurnal variations, the rainfall efficiency of the tower clouds had to exceed that of the mesoscale clouds. When the surface area covered by each cloud type is combined with field experiment results which show that the total precipitation contributions are roughly equal, this provides an estimate of the relative rainfall efficiency of the two cloud types that is in excellent agreement with the field experiment results. Thus, another line of research has been initiated to see whether rainfall estimates from satellite data can be improved by separately measuring the contributions of the two cloud types. These results have now been extended to the whole tropical zone for a period of two years, using the ISCCP cloud climatology results and a new analysis of the differences in convective behavior between El Nino ("disturbed") years and "undisturbed" years. This work will be reported in the thesis of a GRA, within the next year or two.

A more extensive analysis of the variations of the optical thickness of low level and high level clouds in a middle latitude zone under summer and winter conditions, using ISCCP cloud climatology data, confirms the earlier-found relationship between optical thickness (or water content) and temperature inferred from aircraft data for low level clouds over land areas. However, these results also show that the behavior of clouds over oceans is completely different. The relation between cloud water content and optical thickness depends on the vertical extent of clouds as well;

hence isolation of low level clouds in this analysis was crucial. Examination of aircraft measurements suggests that vertical extent variations are not too important for cirrus clouds, either; the satellite results show agreement with these data for the colder temperature range, but not for warmer temperatures. This topic forms the thesis research for one of the GRA's (paper in preparation).

A new cloud parameterization for the GISS climate GCM has been developed, based on a complete water budget (Delgenio and Yao, 1990). A comparison of the new and old GISS cloud properties and variations with the ISCCP results has begun, in order to help constrain poorly-known parameter values in the parameterizations. Two key parameters seem to be 1) a particle size parameter that controls the onset of precipitation in the cloud, and 2) the temperature at which the cloud particles freeze. These two parameters control not only the lifetime of the cloud, but also its water content, which strongly affects the optical thickness of the clouds. Comparisons of the results described above with this new physical cloud model will be made to find an explanation for the differing land-ocean, tropics-midlatitude, cold-warm variation of cloud optical thickness with temperature. A new GRA is pursuing this line of research.

The radiative model of all AVHRR spectral channels has been completed and verified against pilot and field experiment data sets to the extent possible. Also, by exploiting the statistical patterns in the satellite data, associated with the variety of known situations over the globe, the ability of the model to explain the whole range of observed radiation variations has been verified. (This work parallels other research efforts that attempt to validate the radiative transfer models used at

GISS.) From the sensitivity of the model to variations of various cloud parameters, a retrieval scheme has been developed to extend the ISCCP two-wavelength analysis, which obtains cloud optical thickness and top temperature, to a three-wavelength analysis, which also retrieves mean cloud particle size. Application of this method to the ISCCP data base will produce the first global survey of cloud particle sizes.

A radiative transfer model that simulates the whole infrared spectrum of Jupiter's atmosphere has been adapted for application to the Earth's atmosphere. This model includes full scattering effects for infrared wavelengths. (Papers are being prepared to describe the model and its application to Jupiter.) Preliminary comparisons with spectral data, collected in the First ISCCP Regional Experiment - Cirrus, showed excellent ability to measure not only the optical thickness of thin cirrus clouds, but also to detect the presence of two different sized particle populations. These early results supported preparation of a proposal to the Department of Energy for research funding. Further development of this model will give us a better tool for study of the effects of small-scale cloud inhomogeneities.

The first results have been obtained from the total solar and thermal infrared fluxes at the top of the atmosphere and at the surface, using cloud, surface and atmospheric data sets similar to those produced by ISCCP, (Rossow and Lacis, 1990). The more detailed model that uses ISCCP results has been completed and preliminary validation performed by comparison with results from ERBE and a special surface radiation experiment conducted during the FIRE-Cirrus experiment. Both of these comparisons show that the model fluxes agree with independent measurements to within about 20 watts/m^2, on average. More comparisons are underway to elucidate the

detailed differences between the calculated and measured fluxes, including continued participation in an on-going Surface Radiation Pilot Study.

A much simpler method has been developed for calculating surface solar insolation from ISCCP data to be used in studies of the surface biosphere. This work has been done in collaboration with Dr. J. K. Bishop at Lamont-Doherty Geological Observatory. This simpler method can reproduce the full radiative transfer results to within 6 watts/m^2 under all conditions, except over ice and snow covered surfaces. A paper describing this research is in preparation.

Planetary Studies

Two papers on the complete Pioneer Venus record of cloud-tracked winds and large-scale UV brightness fluctuations were published in the past year (Del Genio and Rossow, 1990; and Rossow et al., 1990). A technique was developed to convert Pioneer Venus OCPP polarimetry maps to maps of haze optical thickness anomalies as the first step in tracking polarimetry features at high altitudes.

A parameterization study of Jovian moist convection which places limits on drying due to culumus subsidence and stabilization by latent heat relaese was published (Del Genio and McGrattan, 1990). A manuscript describing the retrieval of solar or super solar water abundance on Jupiter, based on a sophisticated jovian cloud model with realistic cloud radiative properties and relative humidity variations, has been written (Carlson et al., 1990).

PUBLICATIONS
(1989-1990 and in press)

Tasks A and B

Brest, C.L., and W.B. Rossow, 1990: Radiometric calibration and monitoring of NOAA AVHRR data for ISCCP. Int. J. Remote Sensing (in press).

Carlson, B.E., A.A. Lacis, and W.B. Rossow, 1990: The abundance and distribution water vapor in the Jovian troposphere as inferred from Voyager IRIS Observations. Icarus (in preparation).

Cess, R.D., and I.L. Vulis, 1989: Inferring surface solar absorption from broadband satellite measurements. J. Climate, 2, 974-985.

Del Genio, A.D., and K.B. McGrattan, 1990: Moist convection and the vertical structure and water abundance of Jupiter's atmosphere. Icarus, 84, 29-53.

Del Genio, A.D., and W.B. Rossow, 1990: Planetary-scale waves and the cyclic nature of cloud top dynamics on Venus. J. Atmos. Sci.,47, 293-318.

Del Genio, A.D. and M.S. Yao, 1990: Predicting cloud water variations in the GISS GCM. In Preprints, Conference on Cloud Physics, Am. Meteor. Soc., San Francisco, July 23-27, (in press).

Fu, R., A.D. Del Genio, and W.B. Rossow, 1990: Behavior of deep convective clouds in the tropical Pacific deduced from ISCCP radiances. J. Climate (in press).

Gornitz, V., 1990a: Mean Sea-Level Changes in the Recent Past, in R.A. Warrick and T.M.L. Wigley, eds., Climate and Sea Level Change: Observations, Projections and Implications, Cambridge University Press (in press).

Gornitz, V., 1990b: Global coastal hazards from future sea level rise, Global and Planetary Change (in press).

Gornitz, V., 1990c: Vulnerability of the East Coast, U.S.A. to Future Sea Level Change. (Submitted to Skagen Symposium, (Denmark) Sept. 2-5, 1990).

Gornitz, V., 1990d: Impacts of sea level rise on the world's shorelines. Environment (submitted).

Gornitz, V. and L. Seeber, 1990: Vertical crustal movements along the East Coast, North America, from historic and late Holocene sea level data. Tectonophysics, 178, 127-150.

Gornitz, V. and A. Solow, 1990: Observations of long-term tide-gauge records for indications of accelerated sea-level rise, in DOE Workshop on Greenhouse-Gas-Induced Climatic Change: a critical appraisal of simulations and observations, Amherst, Mass., May 8-12, 1989 (in press).

Gornitz, V. and T.W. White, 1990: The Global Coastal Hazards Data Base, in Proc. of the International Workshop on Future Climate Change and Radioative Waste Disposal, U. East Anglia, Norwich, U.K., Nov. 1-3, 1989 (abstract).

Hansen, J., A. Lacis and M. Prather, 1989: Greenhouse effect of chloroflourocarbons and other trace gases. J. Geophys. Res., 94, 16, 417-16,421.

Hansen, J., D. Rind, A. DelGenio, A. Lacis, S. Lebedeff, M. Prather, R. Ruedy and T. Karl, 1989: Regional Greenhouse Climate Effects, in Preparing for Climate Change, Proceedings of the Second North American Conference on Preparing for Climate Change, December 6, 1988, Climate Instutute, Washington, DC.

Jacoby, G.C., Jr. and R. D'Arrigo, 1989: Reconstructed Northern hemisphere annual temperatures since 1671 based on high-latitude tree-ring data from North America, Climatic Change 14, 39-59.

Kneller, M. and D.M. Peteet, 1990: A late glacial pollen and macrofossil record from Brown's Pond, Virginia. AMQUA Abstracts, Waterloo.

Overpeck, J.T., 1989. Lake sediments, climate modeling, and global climate change. Workshop on Large Lakes and Global Climate Change, 24th Congress of the International Association of Theoretical and Applied Limnology, Munich, FRG (Abstract).

Overpeck, J.T. 1990a: Century-to millennium-scale climatic variability during the late Quaternary. In: R. Bradley and J. Eddy, eds., Global Changes of the Past, (in press).

Overpeck, J.T. 1990b. Modeling the transient response of vegetation to climatic change. Transient Responses to Global Change: The Geomorphic and Hydrologic Record, Geological Society of America Symposium, Dallas (Abstract).

Overpeck, J.T., J.D. Anderson, S. Trumbore, W. Wolfli, and W. Press, 1990c. The Southwest Indian Monsoon, the Tibetan Plateau, and abrupt climatic change over the last deglaciation. Beijing International Symposium on Climatic Change, Beijing (Abstract).

Overpeck, J.T., J.D. Anderson, S. Trumbore, W. Wolfli, and W. Prell, 1990d. A new continuous high-resolution record of the SW Indian Monsson and abrupt climatic change over the last deglaciation. Geological Society of America Abstracts with Programs (abstract).

Overpeck, J.T. and P.J. Bartlein, 1989. Assessing the response of vegetation to future climate change: ecological response surfaces and paleoecological model validation in J. B. Smith and D.A. Tirpak, eds., The Potential Effects of Global Climate Change on the United States, U.S. Environmental Protection Agency, Washington, D.C. EPA-230-05-89-50/60.

Overpeck, J.T., B.J. Bartlein, and T. Webb III, 1990a. The magnitude and rate of future vegetation change in eastern North America, Science (in preparation).

Overpeck, J.T. and J.E. Cole, 1990: The role of corals, varved sediments and models in understanding global environmental change. EOS (in press).

Overpeck, J.T., L.C. Peterson, N. Kipp, J. Imbrie, and D. Rind, 1989: Climatic change in the low-latitude North Atlantic region during the last deglaciation. Nature, 338, 553-557.

Overpeck, J.T. and D. Rind, 1989. Climate and biotic change: past, present, and future. The Past as a Key to Understanding Future Global Change, Ecological Society of America Paleoecology Symposium, Toronto (abstract).

Overpeck, J.T., D. Rind, and R. Goldberg, 1990b: Climate-induced changes in forest disturbabce and vegetation. Nature, 343, 51-53.

Peteet, D.M., 1990: Postglacial history of lodgepole pine near Yakutat, Alaska: vegetation-climate in equilibrium? Canadian J. Botany (submitted).

Peteet, D., D. Rind and G. Kukla, 1990: Wisconsin ice sheet initiation -- Milankovitch forcing, paleoclimatic data, and global climate modeling. Bull. Geol. Soc. Amer. (accepted).

Peteet, D.M., J.S. Vogel, D.E. Nelson, J.R. Southon, R.J. Nickmann and L.E. Heusser, 1990: Younger Dryas climatic reversal in northeastern U.S.A.? -- AMS ages for an old problem, Quaternary Research, 33, 219-230.

Peterson, L.C., J.T. Overpeck, N. Kipp, J. Imbrie, and D. Rind, 1989. A high-resolution record of the last deglaciation from the anoxic Cariaco Basin. In Symposium on the Paleoceanography of Marginal Seas, Third International Conference on Paleoceanography, Cambridge, Great Britain (abstract).

Peterson, L.C., J.T. Overpeck, N. Kipp, J. Imbrie, and R. Aparicio, 1990. A high-resolution Late-Quaternary upwelling record from the anoxic Cariaco Basin, Venezuela. Paleoceanography, Special Symposium issue, R. Thunell and M. Cita, eds. (in preparation).

Prather, M., M. Garcia, R. Suozzo and D. Rind, 1990: Global impact of the antarctic ozone hole: dynamical dilution with a 3-D chemical transport model, J. Geophys. Res., 95, 3449-3472.

Reihle, J.R., D.H. Mann, D.M. Peteet, D. Engstrom, and D.A. Brew, 1990: The Mt. Edgecumbe tephra deposits: a late Pleistocene stratigraphic marker in Southeast Alaska. Quaternary Research (submitted).

Rind, D., R. Goldberg, J. Hansen, C. Rosenzweig and R. Ruedy, 1990: Potential evapotranspiration and the likelihood of future drought, J. Geophys. Res., 95 (in press).

Rind, D., G. Kukla, D. Peteet, 1989: Can Milankovitch orbital variations initiate the growth of ice sheets in a GCM? J. Geophys. Res., 94,12, 851-12,871.

Rind, D., C. Rosenzweig and D. Peteet, 1989: African drought: history, possible causes, prognosis. In Africa and Climate Change, P. Molaska, Ed., Cassell Tycooly, pp. 194-218.

Rind, D., R. Suozzo, N.K. Balachandran and M. Prather, 1990: Climate Change and the Middel Atmosphere. Part 1. The doubled CO_2 climate, J. Atm. Sci., 47, 475-494.

Rossow, W.B., C.L. Brest and L.C. Garder, 1989: Global, seasonal surface variations from satellite radiance measurements. J. Climate, 2, 214-247.

Rossow, W.B., A.D. Del Genio and T.P. Eichler, 1990: Cloud-tracked winds from Pioneer Venus OCPP images. J. Atmos. Sci. (in press).

Rossow, W.B., and A.A. Lacis, 1990: Global, seasonal cloud variations from satellite radiance measurements. Part II: Cloud properties and radiative effects. J. Climate (in press).

Rossow, W.B., and R.A. Schiffer, 1990: ISCCP cloud data products. Bull. Amer. Meteor. Soc. (in press).

Seze, G. and W.B. Rossow, 1990a: Time-cumulated visible and infrared histograms used as descriptors of surface and cloud variations. Int. J. Remote Sensing (in press).

Seze, G. and W.B. Rossow, 1990b: Effects of satellite data resolution on measuring the space/time variations of surfaces and clouds. Int. J. Remote Sensing (in press).

Tans, P., I. Fung and T. Takahashi, 1990: Observational constraints on the global atmospheric CO_2 budget. Science, 247, 1431-1438.

Vulis, I.L. and R.D. Cess, 1989: Interpretation of surface and planetary directional albedos for vegetated regions. J. Climate, 2, 986-996.

Webb, R.S., J.T. Overpeck, R.A. Goldberg, and T. Webb III, 1990. Modern analog reconstructions of changes in the vegetation patterns of eastern North America since 18,000 YR B.P. Geological Society of America Abstracts with Programs (abstract).

Yao, M.S. and A.D. Del Genio, 1989: Effects of cumulus entrainment and multiple cloud types on a January global climate model simulation. J. Climate, 2, 850-863.

TASK C: CHEMISTRY OF EARTH AND ENVIRONMENT

As part of the joint Goddard Institute for Space Studies - Lamont-Doherty Geological Observatory program several projects have reached near completion or are well underway.

Two important papers dealing with the results of the GISS - LDGO cooperation were published this past year. The first deals with the comparison between tritium delivery to the ocean in the GISS GCM and observation regarding the actual delivery (Koster et al., 1989). The second concerns interocean transports of water vapor important to coean circulation (Broecker, W.W., T.-H. Peng, et al., 1990).

During the last year, studies have been launched into the pathways by which water vapor is transported in the GISS model from one part of the ocean to another. Studies have also been undertaken of the atmospheric distribution of the radon emitted from continetal soils and the atmospheric distributions and fallout pattern of the lead-210 created by the decay of this radon.

In addition to the work on water vapor and radon, three student research projects have been funded from this Cooperative Agreement during the last year.

1) Jane Warger, a third year graduate student is working on the chemical enhancement of CO_2 exchange across the air-water interface of an alkaline lake. The enchancement of CO_2 exchange across the air-water interface has been experimentally determined for the water of Mono Lake, California. CO_2 gas exchange is enhanced by chemical reactions for the conditions of low turbulence and high pH (9.8) at Mono Lake. Given the enhancement of CO_2,

the average unenhanced gas exchange, and the concentration differences between air and water for the yearly flux of CO_2 can be calculated. The flux of CO_2 is sought, in order to explain the changes in the lake's carbon chemistry, due to the doubling in salinity since the 1940's. Additionally, anomalously high levels of ^{14}C have accumulated in the lake since the 1960's. Therefore, knowledge of the air-water flux would account for the atmospheric contribution to the rise (Broecker, 1988).

The chemical enhancement of CO_2 was experimentally determined in a closed tank by spiking the air phase with CO_2 and the water phase with the unenhanced gas CH_4. The enchancement, which is the ratio of the gas exchange coefficient of CO_2 to CH_4, was determined by monitoring the concentration changes by gas chromatography over time. The experiments were performed over a range of stirring rates, temperatures and salinities.

The experimental results show a nearly linear increase in enhancement with temperature (Figure 1). Existing models of chemical enhancement such as Hoover and Berkshire's (1969) predict a much larger and exponential rise in the enhancement. These models incorporate a strong dependence of enhancement on the rate constants for the chemical reactions of CO_2 with H_2O and hydroxide. Rate constants increase exponentially with temperature according to Arrhenius theory. Therefore, it appears that gas exchange in Mono Lake water depends more highly on diffusion than chemical reaction. Models of chemical enhancement which are based on the film theory of gas exchange do not extrapolate to the high ionic strength and pH of Mono Lake. The mechanism of gas exchange needs to be explored in order to construct a new model. Experiments are required to determine the relationship of diffusion to turbulence. Then the appropriateness of a film replacement or

boundary layer model can be explored (Holmen and Liss, 1984). In addition, the physical chemistry of Mono Lake water needs to be examined especially to determine the concentration of free hydroxide which reacts with CO_2.

While chemical enhancement of CO_2 for Mono Lake water has been quantified for a range of stirring rates, temperatures and salinities, further research is required to fully characterize the nature of both the physical and chemical exchange processes. Constructing a numerical model of gas exchange using an empirically derived exchange coefficient and precise knowledge of the lake's chemistry will further advance the study of CO_2 exchange in alkaline systems.

2) Jordan Clark, a first year graduate student, is evaluating and upgrading a late 1970s multi-box model of the Hudson Estuary. The model predicts nutrient distributions from the freshwater flow, salt profile, and waste water treatment facilities discharge. In the lower Hudson, discharge from treatment facilities scattered around the New York City metropolitan area dominates the nutrient signal.

There are three aspects to this investigation. First, the sensitivity of the model has been evaluated to see whether it can be used to constrain studies of the flow in the lower estuary tidal channels (Kill Van Kull, Arthur Kill, East River, and Harlem River). The second phase of the investigation has used Lamont's historical data set to determine the extent of success of the governmental efforts to improve water quality in the Hudson River. The final part involves upgrading the model to include oxygen.

Preliminary results indicate that the model is not yet sensitive enough to distinguish different flow patterns in the tidal channels, or

whether water quality has improved in the Hudson Estuary, and whether oxygen can be modeled successfully. In order to model oxygen, a number of parameters had to be introduced. In the coming months, it will be determined whether the introduced parameters are real or artifacts of the model, by running a series of laboratory experiments.

3) Jo Lin, a first year graduate student, is conducting research involving two U/Th related projects. One of them is a study of U diffusion in the Black Sea sediments. As the largest anoxic marine basin in the world, the Black Sea basin has sediments enriched in uranium, unlike the other open oceans. Nevertheless, the rapidly deposited turbidite sediments are depleted in uranium compared with the pelagic sediments beneath and above. As time goes on, the uranium should diffuse from the pelagic sediments into the turbidites through the pore water and deposit there. So, measuring the uranium content of the bottom of pelagic sediments, and in the sequence of turbidites, provides a way to study the uranium mobility in the anoxic sediments. This project will be done by α-spectrometry equipment.

The other project is the application of $^{230}Th/^{234}U$ dating to the lacustrine calcium carbonates (tufa) as formed in closed-basin lakes. Tufa is generally believed to be deposited by algae living near the lake level. Tufa is an important clue in studying the lake history and climatic change. Due to the high content of detrital thorium of tufa samples, the isochron drawn from $^{230}Th/^{232}$ ratios versus $^{234}U/^{232}Th$ ratios measured in several samples must be measured. In order to get the variety of calcium carbonate samples needed to produce isochrons, the small sample amount needed mass spectrometry technique is highly advantageous.

PUBLICATIONS

(1989-1990 and in press)

Task C

Broecker, W.S., and G.H. Denton, 1989: The role of ocean-atmosphere reorganizations in glacial cycles, Geochimica et Cosmochimica Acta, 53, 2465-2501.

Broecker, W.S., T.-H. Peng, J. Jouzel and G. Russell, 1990: The magnitude of global fresh water transports of importance to ocean circulation. Climate Dynamics, 4, 73-79.

Broecker, W.S., T.-H. Peng, 1989: The Cause of Glacial to Interglacial Atmospheric CO_2 Change: A Polar Alkalinity Hypothesis. Biogeochemical Cycles, 3,215-239.

Broecker, W.S., S. Trumbore, G. Bonani, W. Wolfli and M. Klas, 1989: Anomalous AMS radiocarbon ages for foraminifera from high deposition rate ocean sediments. Radiocarbon, 31,157-162.

Koster, R., W.S. Broecker, J. Jouzel, R. Suozzo, G. Russell, D. Rind, J.W.C. White, 1989: The global geochemistry of bomb produced tritium; general circulation models compared to real world. Jour. Geophys. Res., 94,18,305-18,326.

T. Takahashi, R. Oxburgh, W.S. Broecker, R. Wanninkhof, and J. Warger, 1990: The carbon budget of Mono Lake, Earth and Planet Sci. Lett., (submitted).

Figure 1: Chemical enhancement which is the ratio of the gas exchange coefficient of CO2 to CH4 is shown for increasing temperature. The modeled curve is from Hoover and Berkshire.

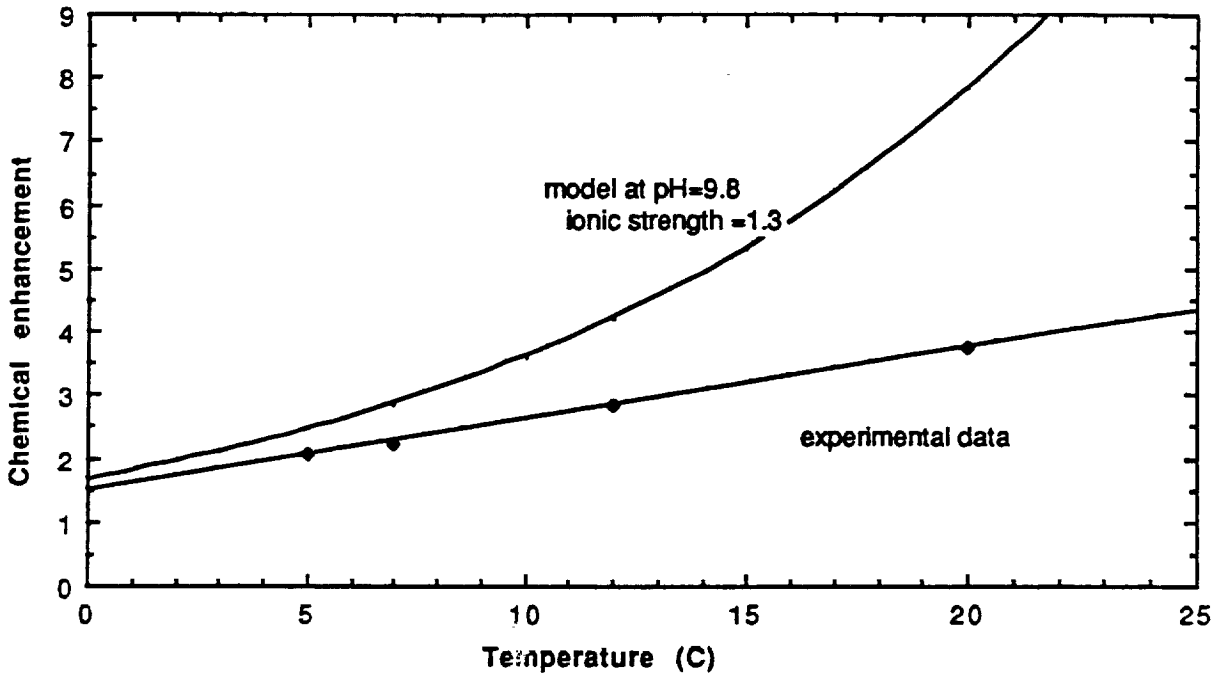

APPENDIX I

Some results for GISS water vapor transport

F. Zaucker

June 8, 1990

This paper is an internal report and must not be cited without previous contacting the author.

Contents

1 Comparison with observations

For comparison with observational data the zonally averaged zonal and meridional water vapor transports are calculated. Those are compared with flux data calculated from a data set of humidity and wind velocities from globally distributed meteorological stations (data from [5], further refered to as GFDL data).

1.1 Zonal transports

The fluxes for each latitude are shown in tables 8 and 9 for the GISS models and the GFDL data set in table 10. Tables 1 and 2 summarize these results.

Table 1: Total zonal transport, in 10^6 g/s eastward

Summer	Fall	Winter	Spring	Average	
91.7	116.9	293.3	130.8	158.2	GISS 8° × 10° grid
104.1	74.1	196.6	147.2	133.6	GISS 4° × 5° grid
270.5	265.7	277.8	274.1	272.0	GFDL data

Table 2: Zonally and yearly averaged zonal transport, in kg/m/s, eastward

lat < 90°S	24°S ≤ lat ≤ 24°N	lat > 24°N	
43.4	−64.3	26.6	GISS 8° × 10° grid
49.2	−142.1	33.0	GISS 4° × 5° grid
59.0	−82.5	40.4	GFDL data

As can be seen from figure Z1 and tables 1 and 2 the eastward water vapor transport in the mid latitudes is too low in the GISS 8° × 10° model whereas the GISS 4° × 5° model comes closer to the observational data in the yearly average. In the tropics however the 4° × 5° grid model has a much higher westward transport than both the 8° × 10° grid model and the GFDL data. 8° × 10° grid and GFDL data show mainly the same transport in this latitude although the model has a narrower peak which seems to be shifted of the order of ten degree south. A closer look on the seasonal distribution of water fluxes shows (figures Z2–Z5), that the main difference in the tropics between the models and GFDL data occurs in summer. While

the 4° × 5°grid model does a fairly good job in mid latitudes the 8° × 10° resolution model tends to underestimate those fluxes.

The tropics are known to be a very critical region in GCMs including the GISS model and the implications of this problem on our calculations will have to be investigated.

1.2 Meridional transports

Tables 11 and 12 show the zonally averaged meridional transports for each latitude. The latitudinal distribution of the meridional fluxes are plotted in figures M1 to M5 for each season and for the yearly average. It can be seen that both model resolutions overestimate the meridional transports in mid and high latitudes. The difference between the GFDL data and the model results is bigger in the 4° × 5° model than it is in the 8° × 10° resolution.

2 Interbasin transport

For studying the transport between the two major ocean basins (Atlantic and Pacific/Indian Ocean) the drainage boundary had to be defined in the resolution of the GCMs. This was done by relating river runoffs to the individual grid boxes. The transport of water vapor across these boundaries was examined for the American Continent (mainly following the Andes and Rockies) as well as the boundary in Africa and Asia (see figures M1 and M2). The results of these calculations for the 8° × 10° and 4° × 5° grid models are summarized in table 3 and 4.

Table 3: Interbasin water vapor transport in Sverdrup (1 Sv = 10^6 m^3/s), GISS 8° × 10°grid. Positiv fluxes are from the Pacific to the Atlantic basin.

	America	Asia	Southern Ocean	Total
Juli	-0.482	0.256	-0.108	-0.334
October	-0.140	0.068	-0.155	-0.227
January	0.067	0.124	-0.015	0.176
April	-0.077	0.135	-0.072	-0.014
Yearly average	-0.158	0.146	-0.088	-0.1

The yearly average of about 0.3 Sv of water vapor being transported from the Atlantic to the Pacific. This result is in the same range as the estimates of several authors from other sources (see for example [2] and table 5).

Table 4: Interbasin water vapor transport in Sverdrup ($1\,Sv = 10^6\,m^3/s$), GISS 4° × 5°grid. Positiv fluxes are from the Pacific to the Atlantic basin.

	America	Asia	Southern Ocean	Total
Summer[a]	-0.369	-0.103	-0.153	-0.625
Fall[b]	-0.0176	0.165	-0.165	-0.0176
Winter[c]	-0.389	0.375	-0.222	-0.236
Spring[d]	-0.391	0.253	-0.138	-0.276
Yearly average	-0.292	0.172	-0.169	-0.289

[a] June, Juli, August
[b] September, October, November
[c] December, January, February
[d] March, April, May

Table 5: Atmospheric water vapor transport form the Atlantic to the Pacific and Indian, comparison of different methods

	A →P/I [Sv]	source
Baumgartner and Reichel Climatology	0.45	[2]
GISS water budget calculations	0.26	[2]
Pandora Ocean box model	0.25	[2]
Manabe and Stouffer Ocean GCM	0.45	[1]
GISS 8° × 10° water vapor transport	0.1	this study
GISS 4° × 5° water vapor transport	0.29	this study

Also included in table 5 is the transport across 40° N in the North Atlantic. This boundary separates a region where evaporation exceeds precipitation and runoff from a region with the reversed situation. The atmospheric water vapor flux to the north can dilute the salt content of the surface water and therefor counteract the mechanism which generates North Atlantic Deep Water.

2.1 Sensitivity

To test the sensitivity of the interbasin transports to the definition of the basin boundaries the same calculations have been made with the boundaries shifted one grid box in different directions. The results for the 8° × 10° and 4° × 5° model are shown in tables 6 and 7 respectively.

Table 6: Sensitivity of interbasin water vapor transport, GISS 8°×10°. Units are Sverdrup. Positiv fluxes are from the Pacific to the Atlantic basin.

	−1	±0	+1	dir	mean
America	−0.149	−0.158	−0.215	x	−0.152 ± 0.06
America	−0.048	−0.158	−0.190	y	
Asia	−0.047	0.146	0.120	x	0.042 ± 0.087
Asia	0.015	0.146	−0.025	y	
Southern Ocean	−0.170	−0.088	−0.001	y	−0.086 ± 0.085
Total					−0.196 ± 0.136

Table 7: Sensitivity of interbasin water vapor transport, GISS 4°×5°. Units are Sverdrup. Positiv fluxes are from the Pacific to the Atlantic basin.

	−1	±0	+1	dir	mean
America	−0.243	−0.292	−0.368	x	−0.291 ± 0.06
America	−0.225	−0.292	−0.328	y	
Asia	0.196	0.172	0.236	x	0.202 ± 0.04
Asia	0.212	0.172	0.195	y	
Southern Ocean	−0.164	−0.169	−0.134	y	−0.156 ± 0.019
Total					−0.245 ± 0.075

The comparison of the sensitivity test for the two model resolutions shows that the the accuracy of the result does strongly depend on the model

resolution. While the estimated error of $\approx \pm 30$ % for the $4° \times 5°$ grid model is reasonable, the error of more than ± 63 % for the $8° \times 10°$ resolution would make the result of this calculations much more questionable.

2.2 Vertical structure

Figures AM1 to AM10 and AS1 to AS10 show the latitudinal and vertical structure of the water fluxes across the American and African/Asian drainage boundaries. The main part of the model transports occurs in the first five model layers with the maximum in layers 2 and 3. In the region of the Andes there is an inverted flux in the first two layers compared to the vertically integrated transport.

3 Conclusions

The work done so far shows that

- atmospheric water vapor transport can be modeled reasonably good by global circulation models,
- the GISS $4° \times 5°$ grid model is doing better in mid and high latitudes than the $8° \times 10°$ resolution model,
- the tropics are a critical region for the model transports and the model has to be improved there,
- the models estimate of water vapor transport from the Pacific/Indian drainage basin to the Atlantic is about 0.3 Sverdrup and agrees with other estimates.

4 Perspectives

4.1 Observations

The comparison of the model results with real world dat is very important for understanding the reliability of model results, especially if climatological experiments are being done. We are currently investigating the availability of other indepent and eventually more recent sets of meteorological data. For that purpose we are in contact with the National Meteorological Center (NMC) in Maryland, the European Center for Midrange Weather Forecast

(ECMWF) in Great Britain, and the Max Planck Institute for Meteorology (Hamburg, West Germany).

4.2 Model development

GISS is currently investigating the influence of a different numeric scheme on model performance. Other improvements in various parts of the model, e.g. parametrization of clouds, ground hydrology, vegetation ... will affect the reliability of the model results.

Especially in mountain regions with steep elevation changes the averaged model topography is far away from the real world. Sensitivity experiments will be done to study the influence of this effect on the hydrological cycle. For that purpose the vertical distribution and the reginal structure of the model transports will have to be studied.

It is hoped that for example the model's tropical transports will be more realistic in the future.

4.3 Climate experiments

A run of the 4° × 5° grid model with double atmospheric CO_2 content (relative to todays conditions) was made and is awaiting evaluation. Another run simulating ice age climate is planned. These runs will be used to study the variation of atmospheric water vapor transport under changing climatic conditions. The impacts of the fresh water transport between the Atlantic and the Pacific and Indian oceans on the salt budget will be investigated. Hopefully this will give further insight into the driving forces for the global ocean circulation.

Appendix

Table 8: Zonally averaged zonal transport, GISS 8° × 10° model, in kg/m/s eastward

	Summer	Fall	Winter	Spring	Average
2	0.0	-3.3	0.0	-5.0	-2.1
3	0.0	5.5	0.0	0.0	1.4
4	18.0	18.1	5.0	0.0	10.3
5	57.0	54.5	84.0	68.0	65.9
6	66.0	73.5	123.0	105.0	91.9
7	64.0	71.0	114.0	86.0	83.8
8	64.0	62.3	64.0	57.0	61.8
9	61.0	57.1	0.0	18.0	34.0
10	-11.0	0.3	-27.0	-39.0	-19.2
11	-141.0	-99.8	-13.0	-73.0	-81.7
12	-250.0	-140.5	-34.0	-130.0	-138.6
13	-98.0	-88.2	-121.0	-118.0	-106.3
14	57.0	-7.2	-123.0	-61.0	-33.6
15	32.0	-26.6	-41.0	10.0	-6.4
16	43.0	17.6	71.0	61.0	48.1
17	21.0	36.1	59.0	46.0	40.5
18	7.0	25.0	59.0	53.0	36.0
19	36.0	34.0	50.0	41.0	40.2
20	33.0	20.6	30.0	18.0	25.4
21	23.0	14.8	16.0	7.0	15.2
22	14.0	4.8	5.0	0.0	6.0
23	5.0	-0.8	2.0	0.0	1.6
Total	4.6	5.8	14.7	6.5	7.9
Global [10^6 kg/s]	91.7	116.9	293.3	130.8	158.2

Table 9: Zonally averaged zonal transport, GISS 4° × 5° model, in kg/m/s eastward

	Summer	Fall	Winter	Spring	Average
1	0.0	0.0	0.0	0.0	0.0
2	-3.2	-2.8	-3.7	-2.2	-3.0
3	-2.7	0.0	1.2	-1.5	-0.8
4	-2.1	-1.9	-1.8	-1.0	-1.7
5	-2.9	-4.9	-5.6	-0.1	-3.4
6	-4.6	-4.2	-0.9	6.8	-0.7
7	-3.5	-4.1	10.7	21.0	6.0
8	14.8	10.1	47.7	54.6	31.8
9	34.8	33.0	87.0	83.0	59.5
10	49.8	56.3	128.0	102.0	84.0
11	66.1	86.1	161.0	116.0	107.0
12	84.3	117.0	177.0	113.0	123.0
13	104.0	141.0	163.0	92.6	125.0
14	125.0	160.0	128.0	62.1	119.0
15	140.0	149.0	79.9	30.4	99.7
16	128.0	110.0	23.4	-1.9	64.8
17	100.0	62.3	-30.7	-30.0	25.5
18	45.0	-2.0	-69.9	-56.8	-20.9
19	-38.3	-65.1	-89.6	-74.1	-66.8
20	-125.0	-123.0	-88.4	-75.1	-103.0
21	-217.0	-178.0	-99.6	-99.7	-149.0
22	-288.0	-225.0	-146.0	-136.0	-199.0
23	-306.0	-207.0	-160.0	-144.0	-204.0
24	-284.0	-209.0	-234.0	-206.0	-233.0
25	-186.0	-167.0	-314.0	-218.0	-221.0
26	-91.9	-117.0	-319.0	-199.0	-182.0
27	-65.9	-142.0	-314.0	-158.0	-170.0
28	-37.5	-124.0	-199.0	-92.4	-113.0
29	0.1	-83.8	-65.6	-23.2	-43.1
30	18.4	-43.5	52.1	37.9	16.2
31	21.4	1.0	123.0	74.0	54.9
32	51.0	44.8	136.0	81.0	78.2
33	62.7	72.5	127.0	75.7	84.4
34	73.0	89.0	102.0	63.7	82.0
35	70.0	103.0	78.9	54.2	76.4
36	51.2	97.2	49.4	43.9	60.4
37	35.5	80.4	20.4	32.1	42.1
38	33.6	51.8	2.6	20.2	27.0
39	42.3	31.5	-0.9	13.8	21.7
40	52.4	27.2	1.9	10.2	22.9
41	45.8	20.0	5.8	7.6	19.8
42	33.6	11.4	4.3	3.8	13.3
43	15.3	6.8	3.2	0.0	0.0
44	-9.0	2.7	-2.7	-2.2	-2.8
45	-70.3	-30.2	-21.0	-17.8	-34.8
46	0.0	0.0	0.0	0.0	0.0

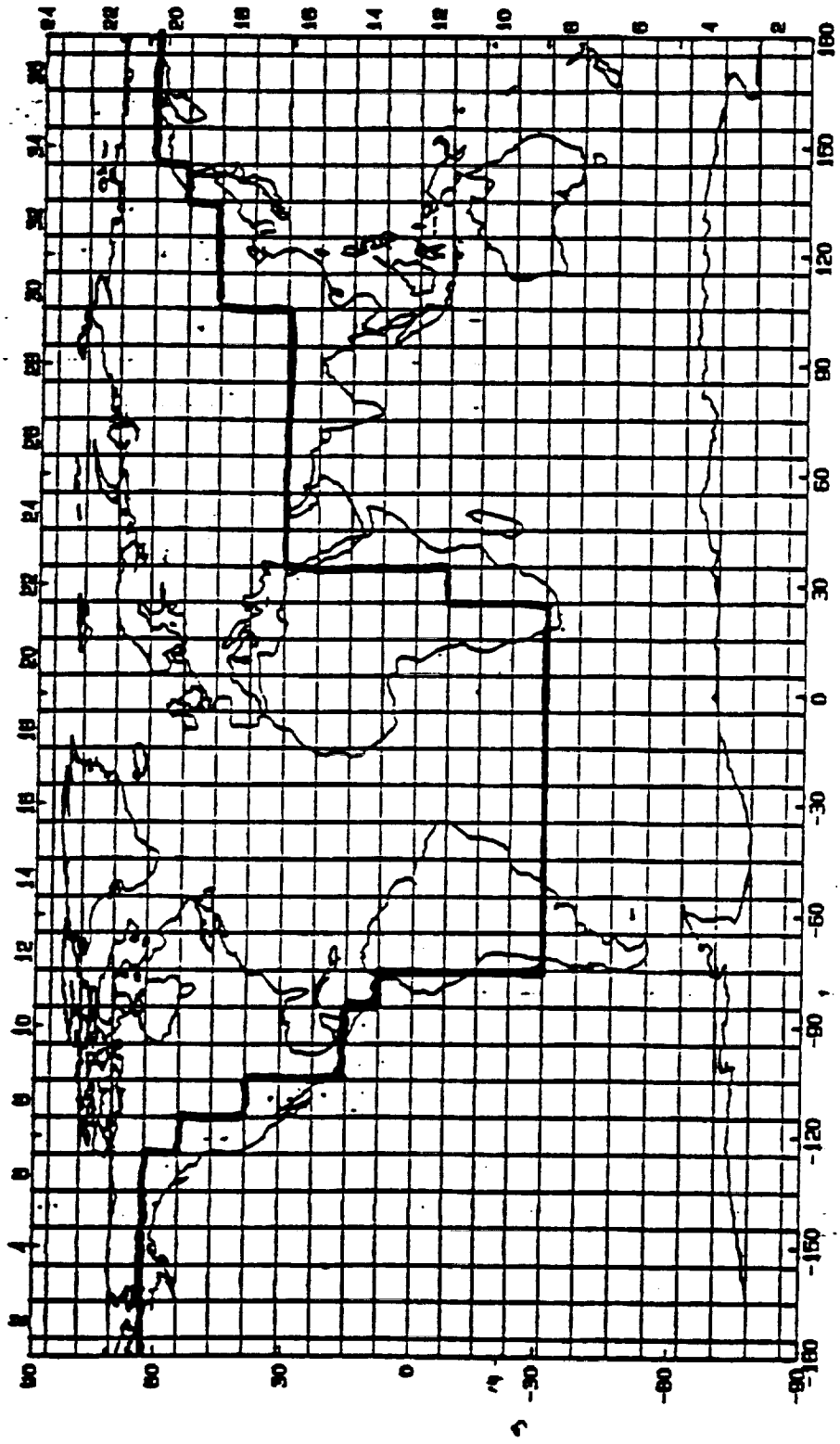

the GISS 8°x10° model

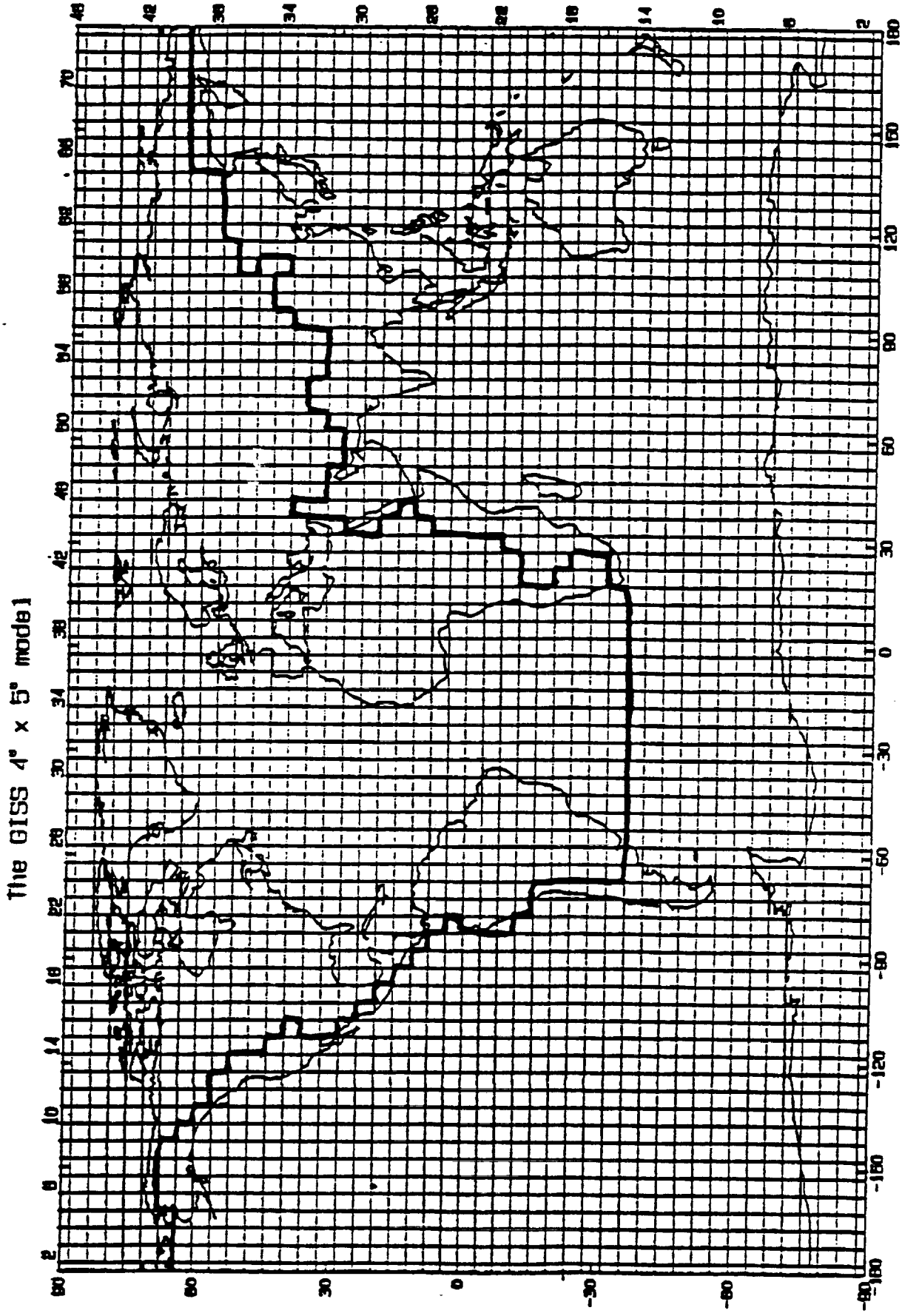

fig 21

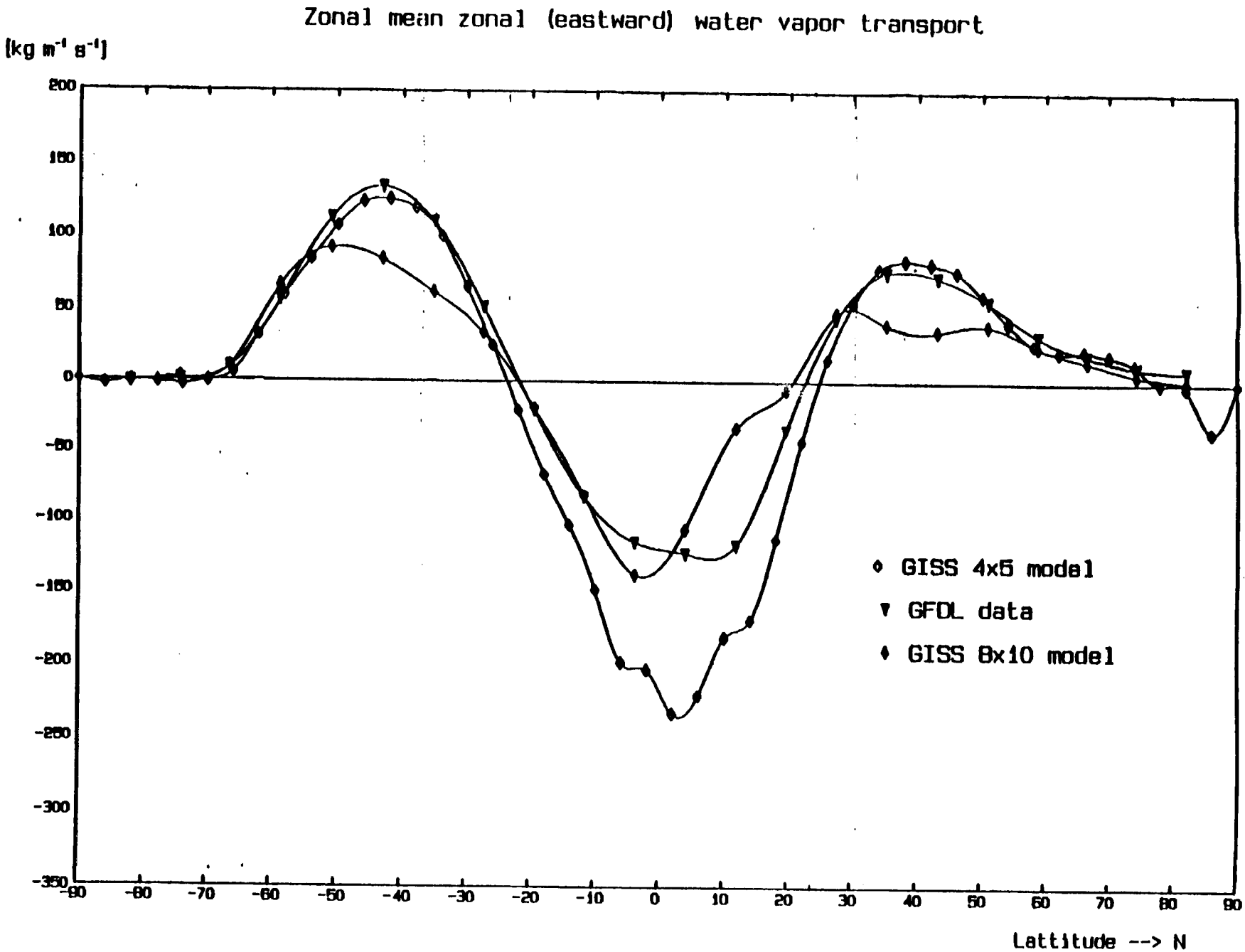
Zonal mean zonal (eastward) water vapor transport
[kg m⁻¹ s⁻¹]
200
150
100
50
0
-50
-100
-150
-200
-250
-300
-350
-90 -80 -70 -60 -50 -40 -30 -20 -10 0 10 20 30 40 50 60 70 80 90
Lattitude --> N
GISS 4x5 model
GFDL data
GISS 8x10 model

fig 22

Sum

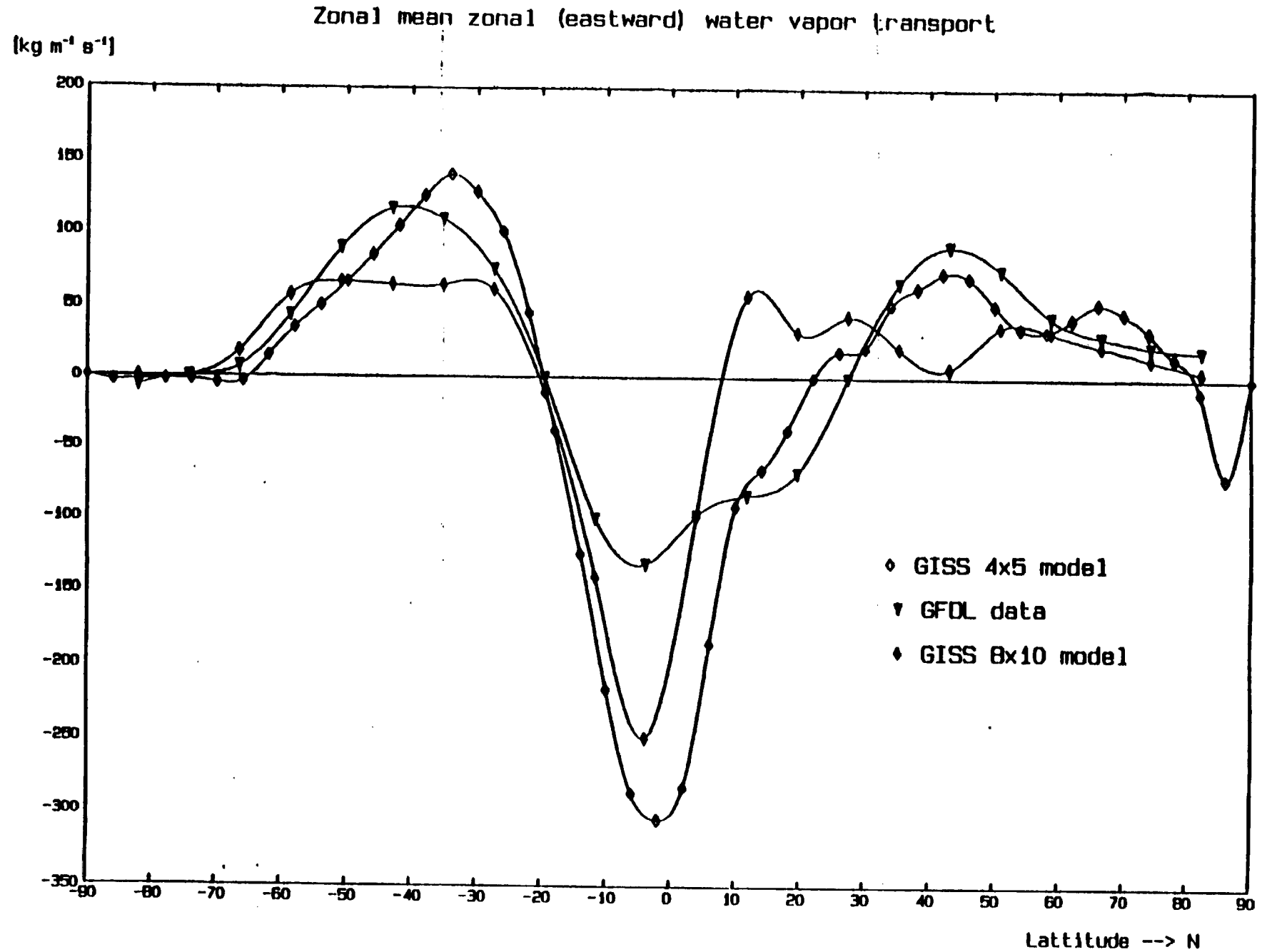
Zonal mean zonal (eastward) water vapor transport
[kg m⁻¹ s⁻¹]
200
150
100
50
0
-50
-100
-150
-200
-250
-300
-350
-90 -80 -70 -60 -50 -40 -30 -20 -10 0 10 20 30 40 50 60 70 80 90
Lattitude --> N
GISS 4x5 model
GFDL data
GISS 8x10 model

Fig 24

Spr
win

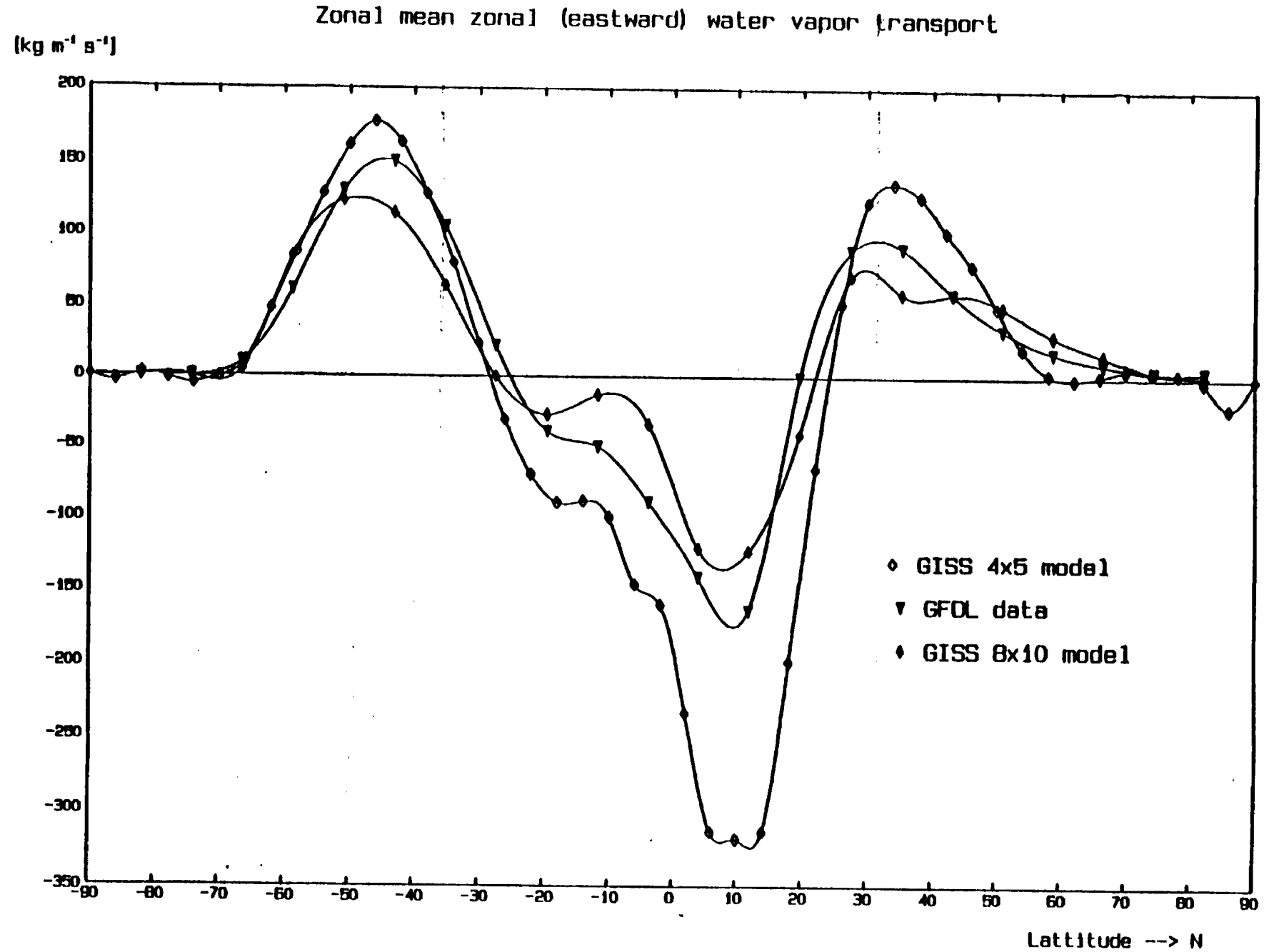

Fig 23

Zonal mean zonal (eastward) water vapor transport

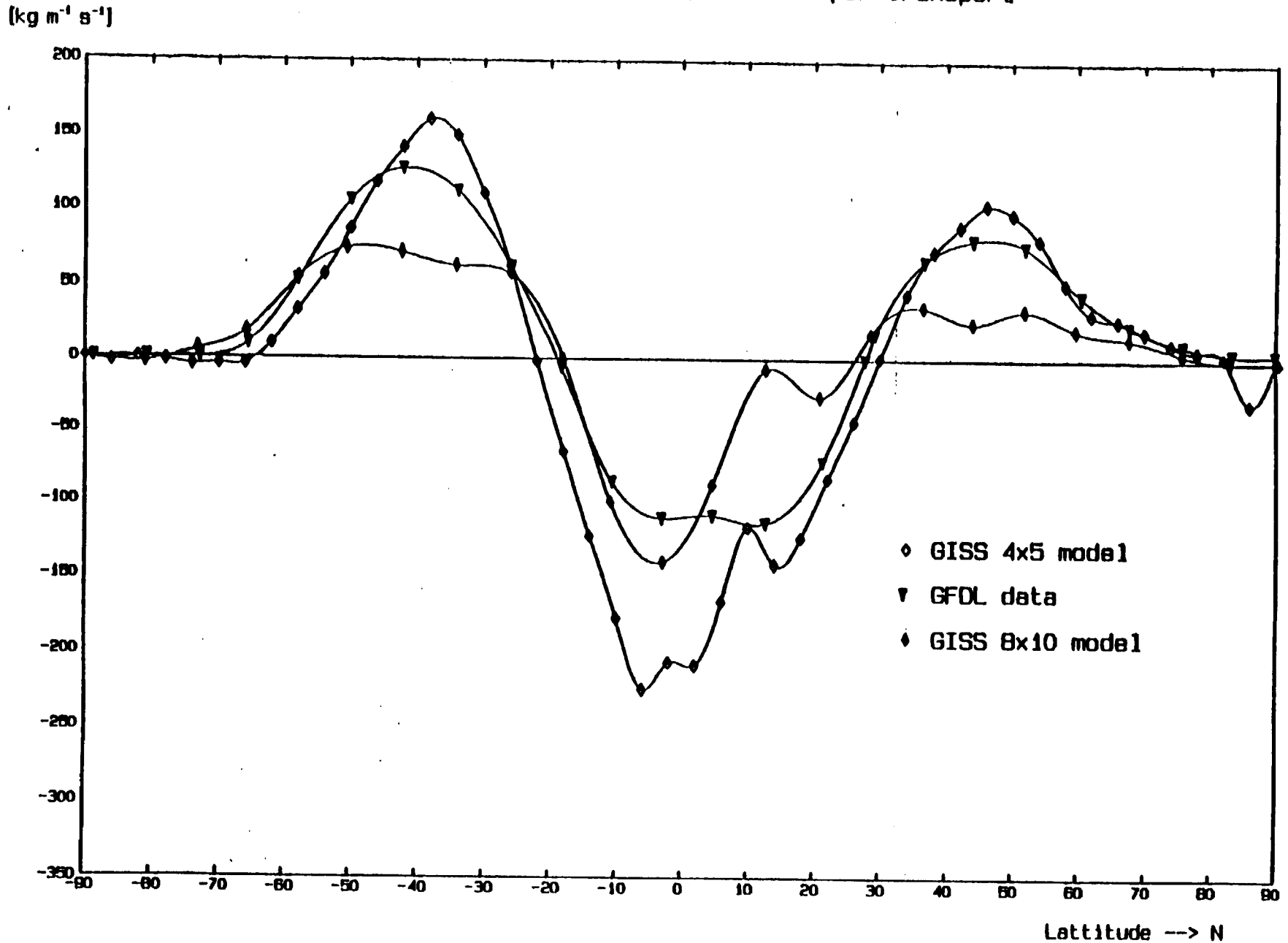

Fig 25

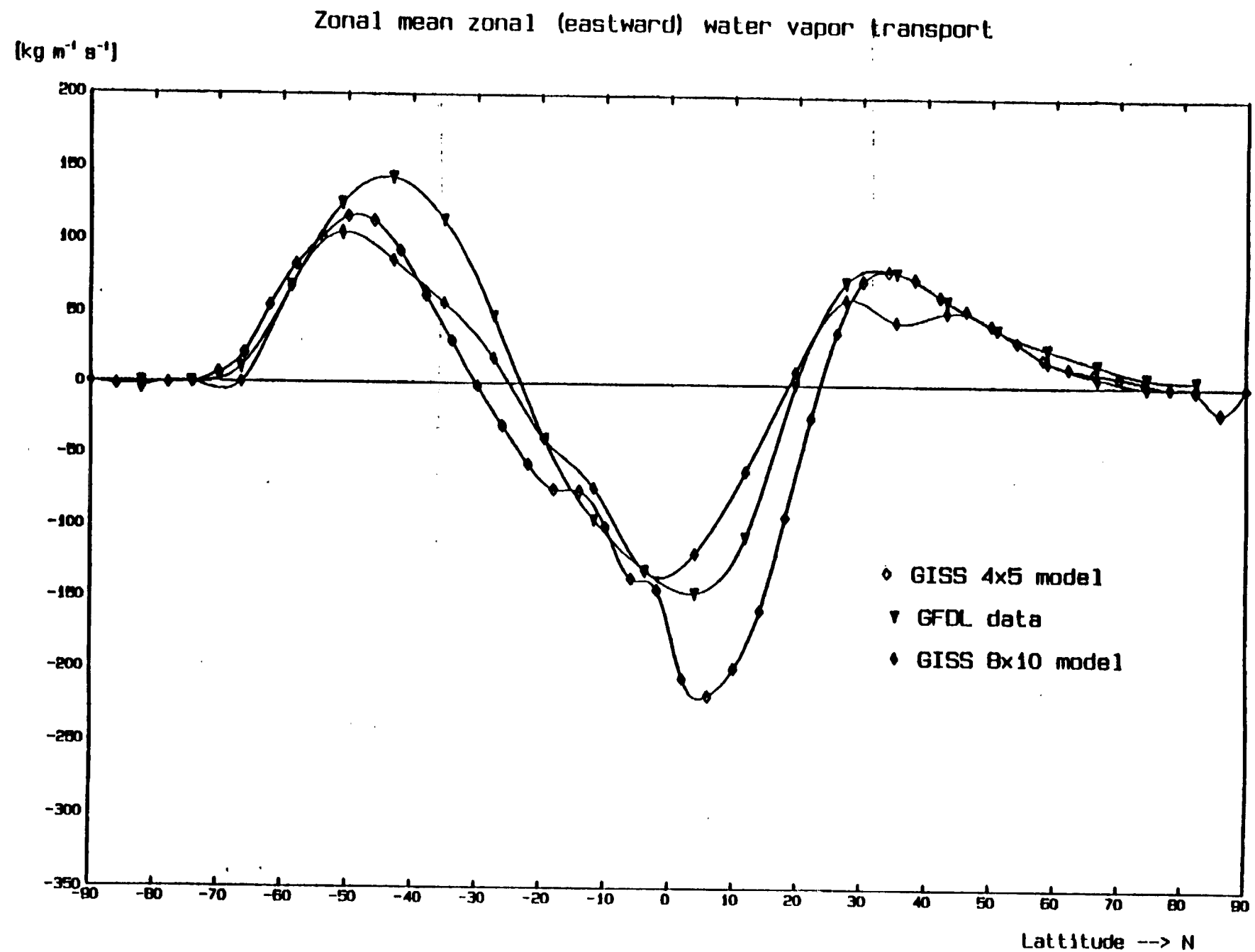
Zonal mean zonal (eastward) water vapor transport
[kg m⁻¹ s⁻¹]
200
100
0
-100
-200
-300
-350
-90 -80 -70 -60 -50 -40 -30 -20 -10 0 10 20 30 40 50 60 70 80 90
Lattitude --> N
GISS 4x5 model
GFDL data
GISS 8x10 model

Fig 11

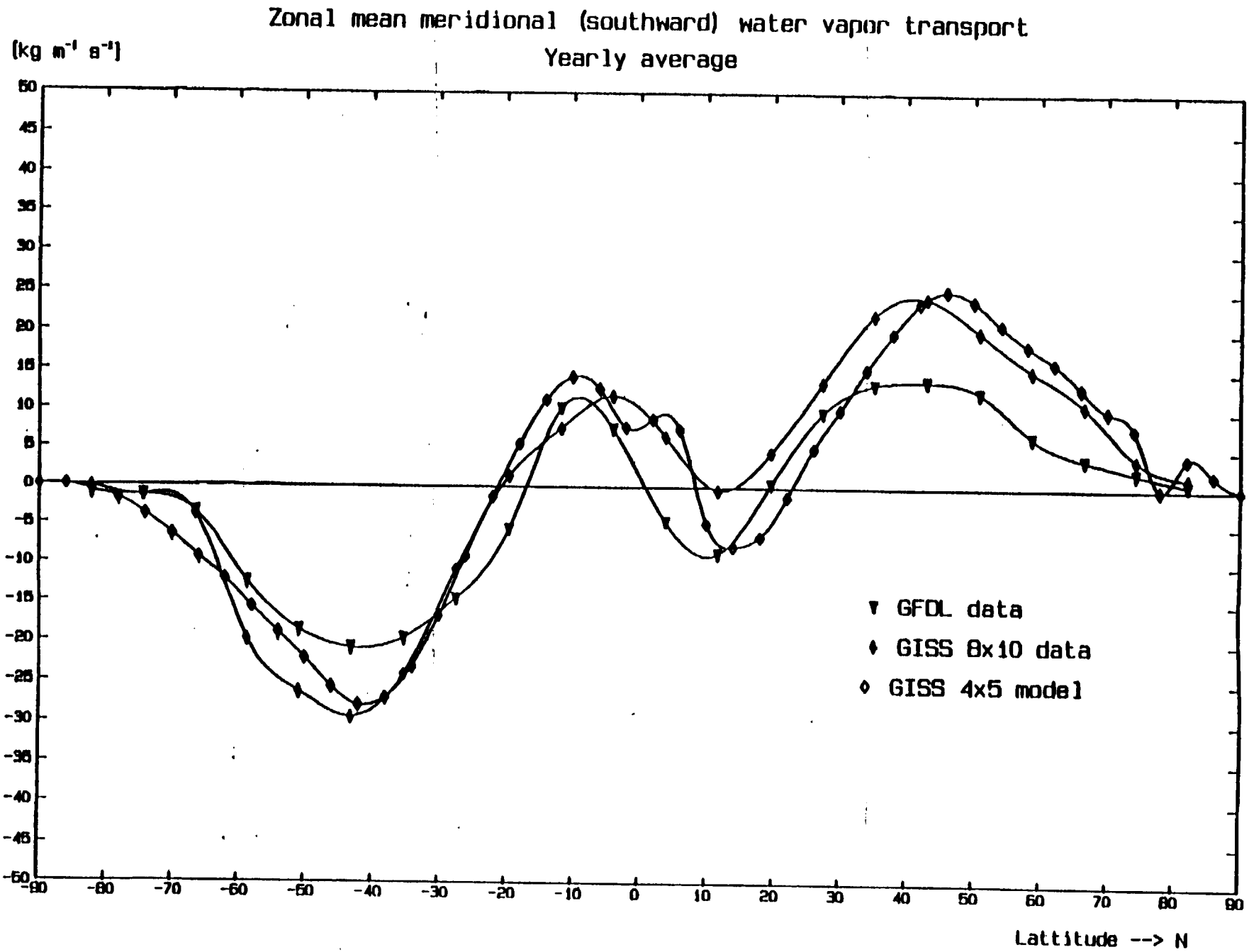
Zonal mean meridional (southward) water vapor transport
Yearly average
[kg m⁻¹ s⁻¹]
60
45
40
35
30
25
20
15
10
5
0
-5
-10
-15
-20
-25
-30
-35
-40
-45
-50
-90 -80 -70 -60 -50 -40 -30 -20 -10 0 10 20 30 40 50 60 70 80 90
Lattitude --> N
GFDL data
GISS 8x10 data
GISS 4x5 model

Fig 12

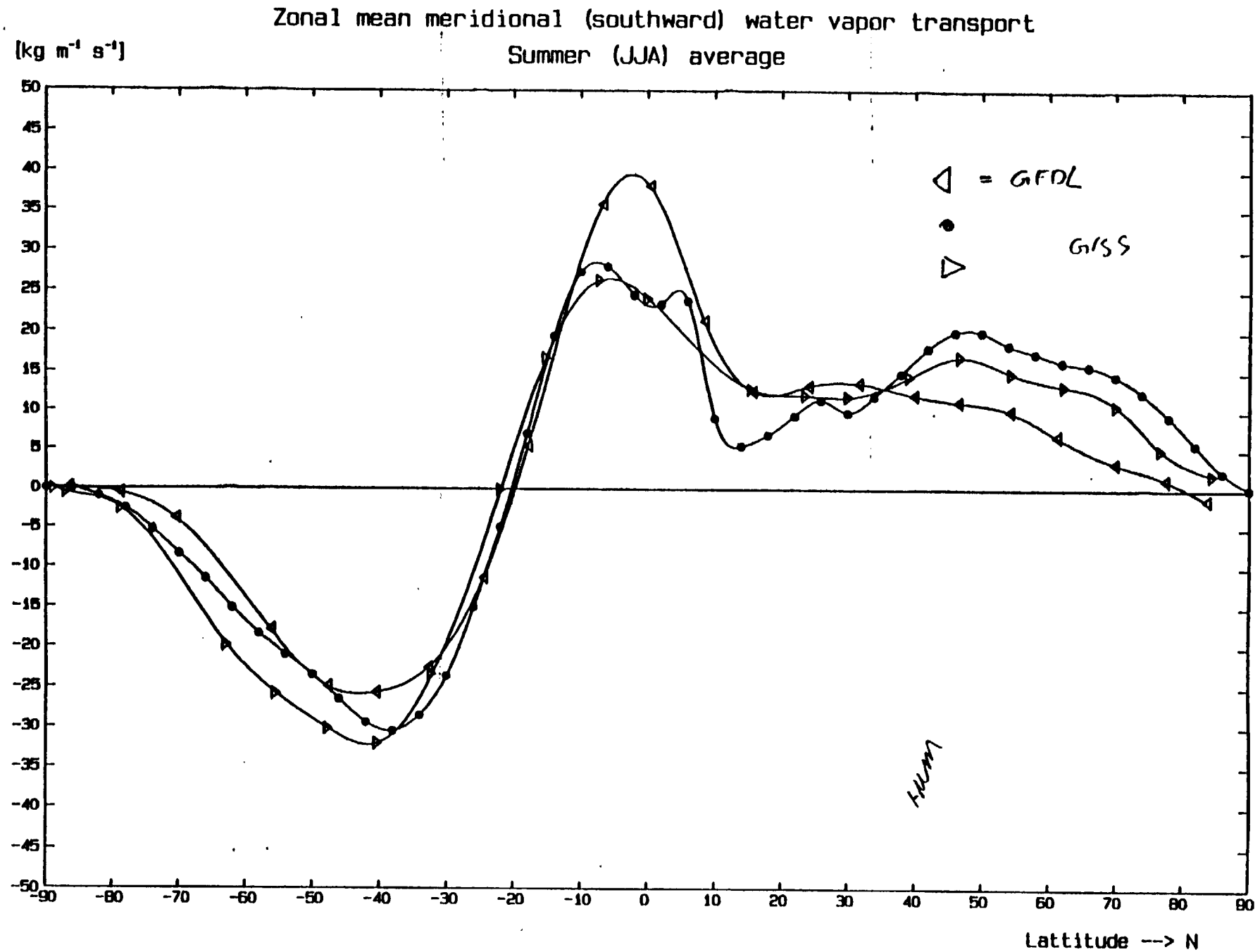
Zonal mean meridional (southward) water vapor transport
Summer (JJA) average
[kg m⁻¹ s⁻¹]
◁ = GFDL
● GISS
▷
50
45
40
35
30
25
20
15
10
5
0
-5
-10
-15
-20
-25
-30
-35
-40
-45
-50
-90 -80 -70 -60 -50 -40 -30 -20 -10 0 10 20 30 40 50 60 70 80 90
Lattitude --> N

Fig 14

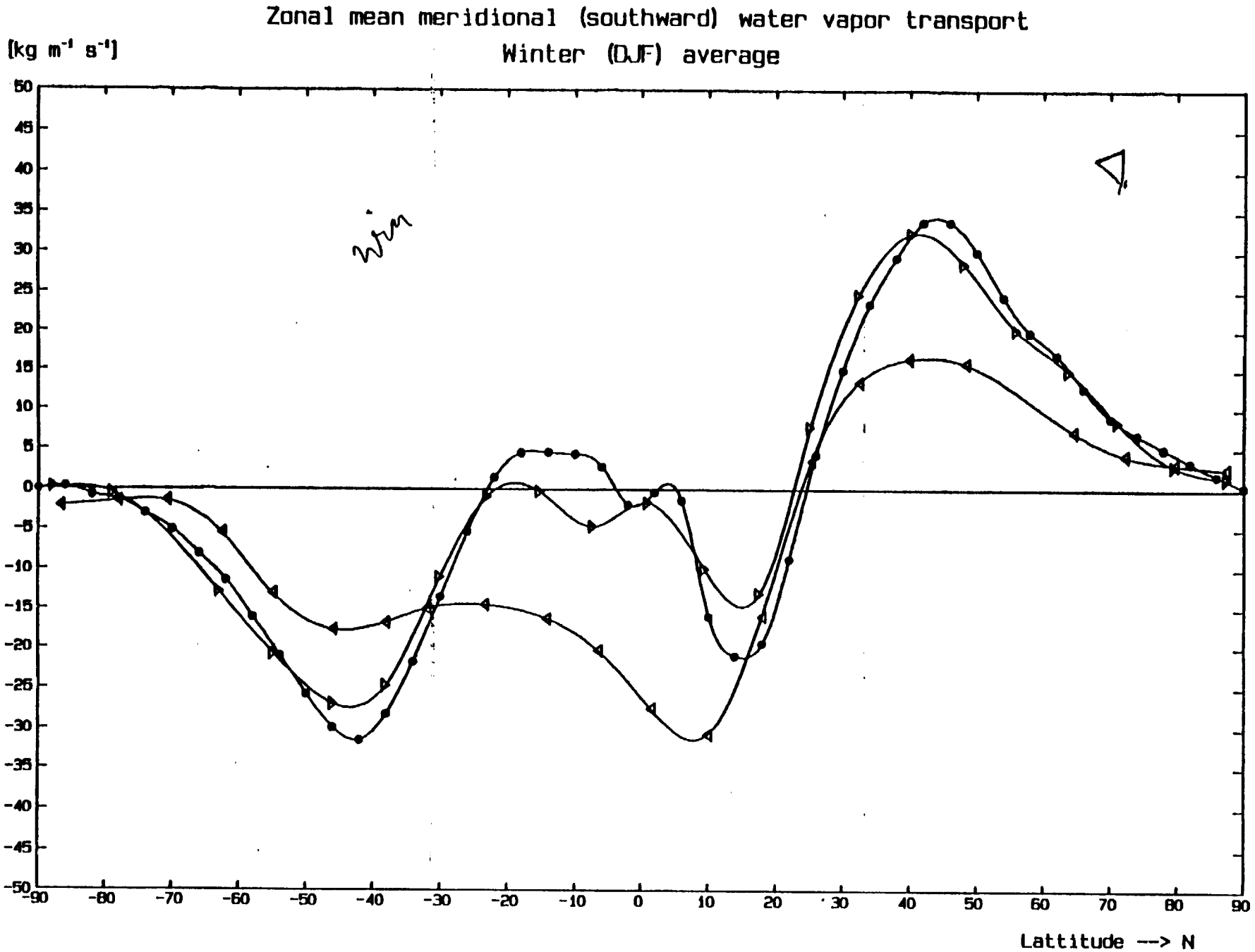
Zonal mean meridional (southward) water vapor transport
Winter (DJF) average
[kg m⁻¹ s⁻¹]
50
45
40
35
30
25
20
15
10
5
0
-5
-10
-15
-20
-25
-30
-35
-40
-45
-50
-90 -80 -70 -60 -50 -40 -30 -20 -10 0 10 20 30 40 50 60 70 80 90
Lattitude --> N

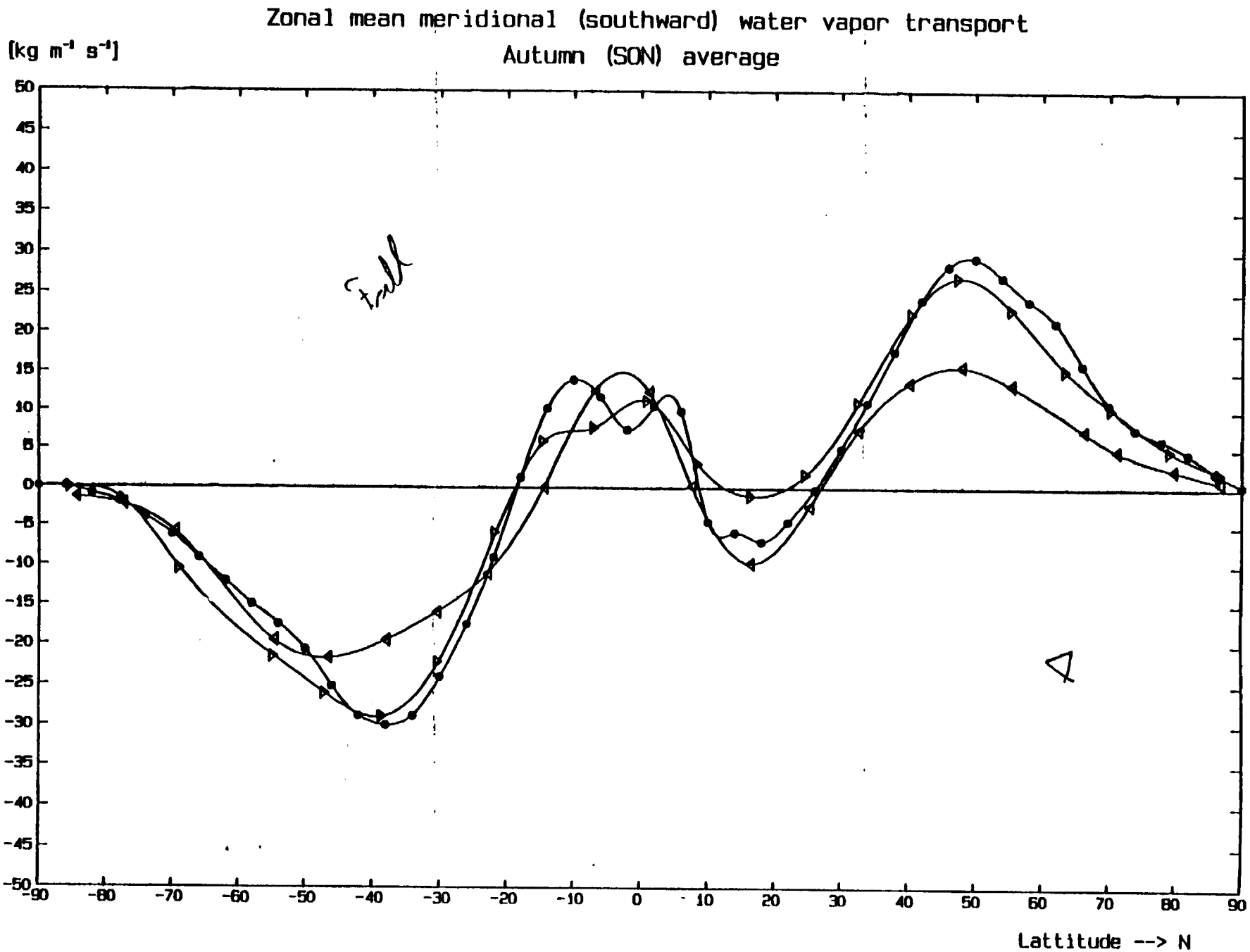
Zonal mean meridional (southward) water vapor transport
Autumn (SON) average
[kg m⁻¹ s⁻¹]
50
45
40
35
30
25
20
15
10
5
0
-5
-10
-15
-20
-25
-30
-35
-40
-45
-50
-90 -80 -70 -60 -50 -40 -30 -20 -10 0 10 20 30 40 50 60 70 80 90
Lattitude --> N

Zonal mean meridional (southward) water vapor transport

[kg m^{-1} s^{-1}]

Spring (MAM) average

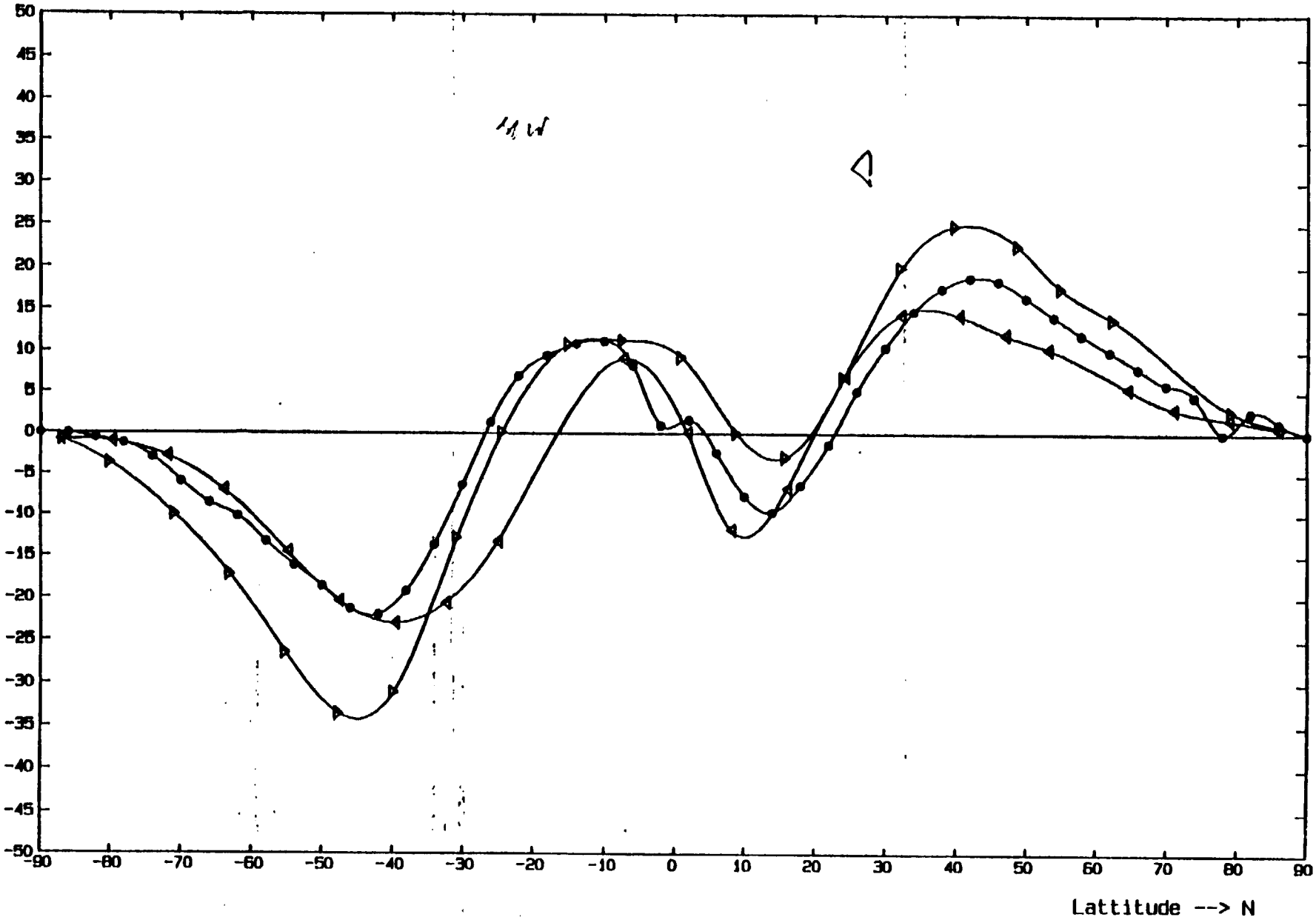

fig AS1 - 1540

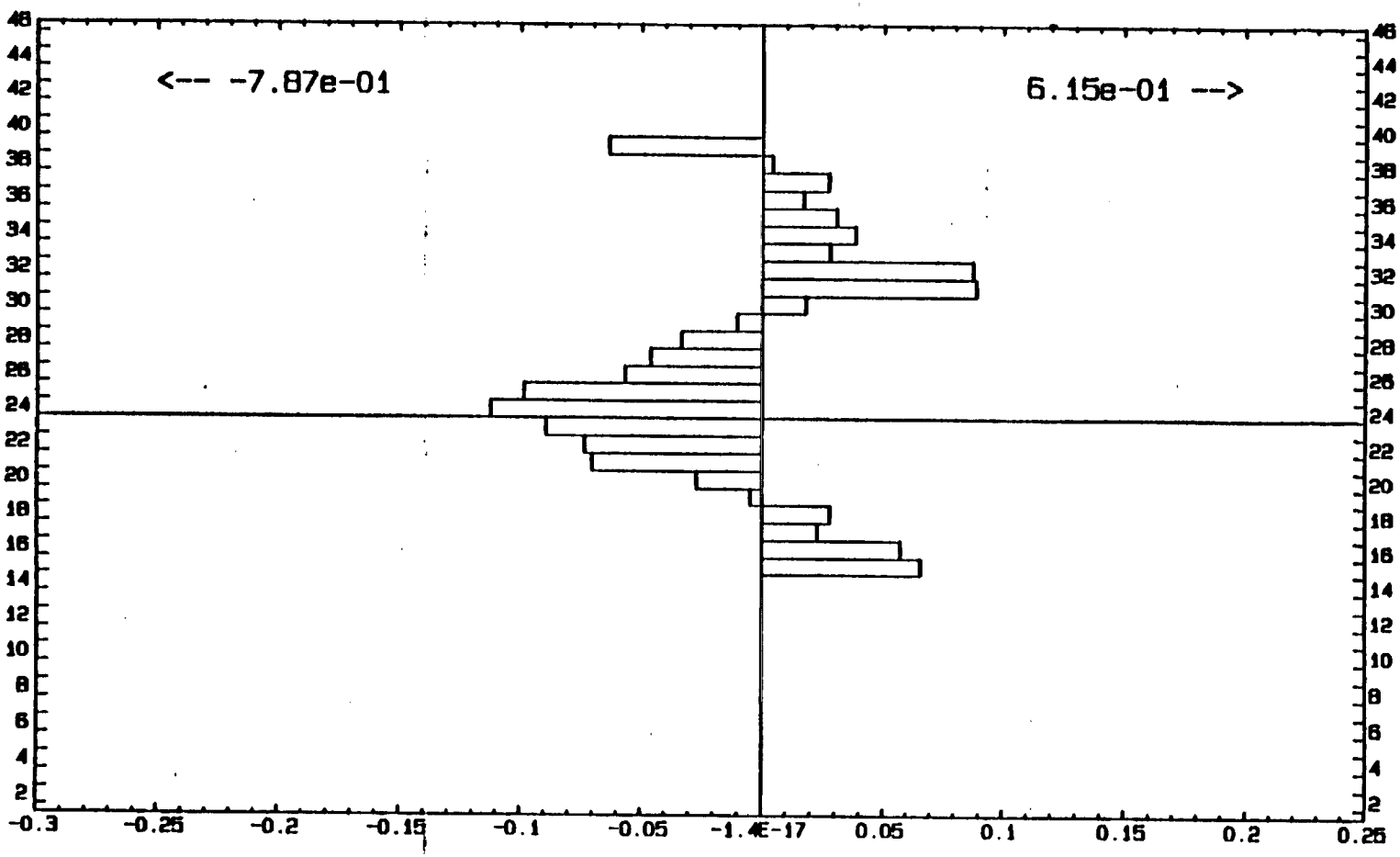
H₂O transport across the African/Asian Cordillera, GISS 4°x5°
Ave @year, layer 0, total: -1.72e-01
<-- -7.87e-01
6.15e-01 -->
46
44
42
40
38
36
34
32
30
28
26
24
22
20
18
16
14
12
10
8
6
4
2
-0.3
-0.25
-0.2
-0.15
-0.1
-0.05
-1.4E-17
0.05
0.1
0.15
0.2
0.25

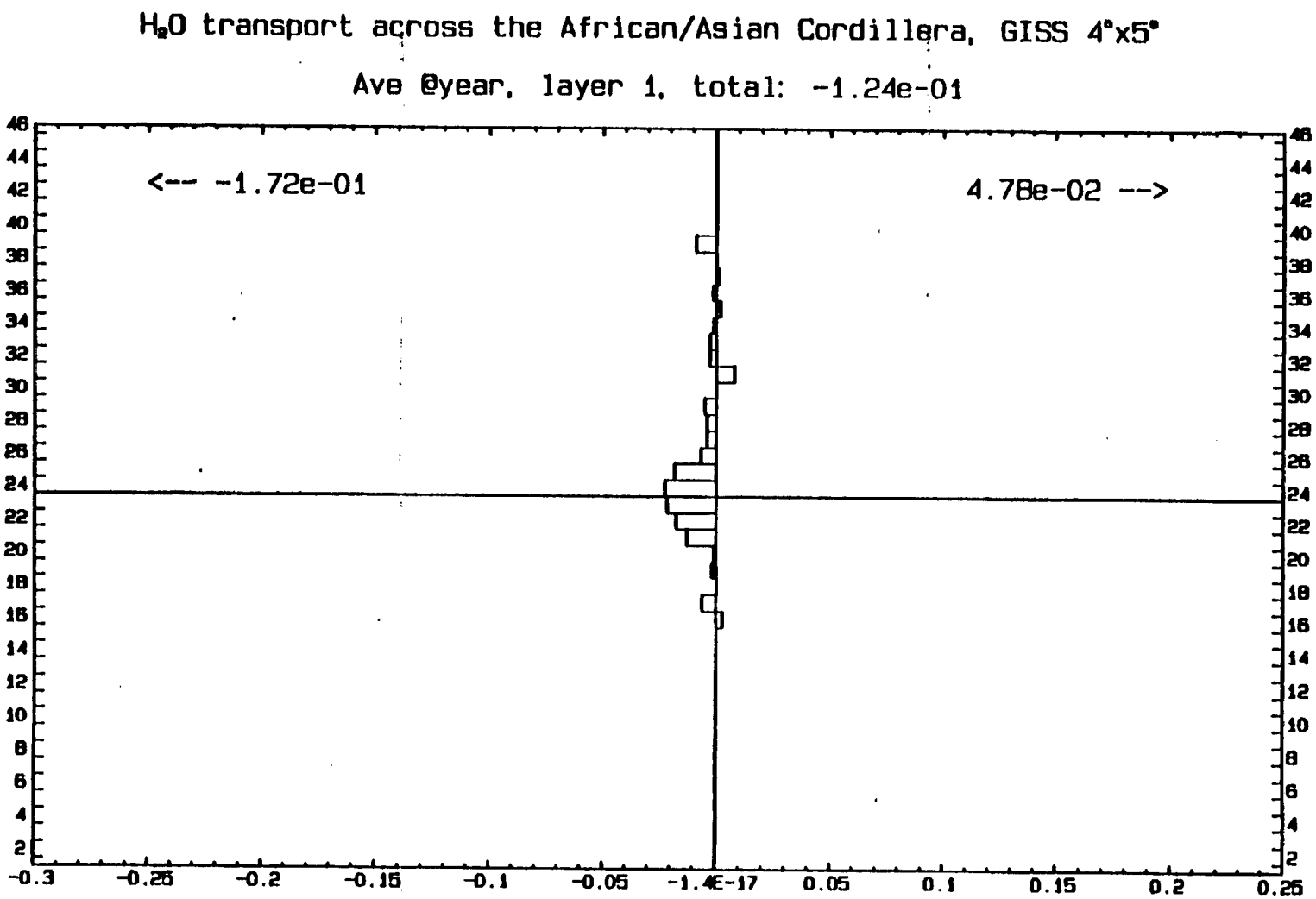
H2O transport across the African/Asian Cordillera, GISS 4°x5°
Ave @year, layer 1, total: -1.24e-01
<-- -1.72e-01
4.78e-02 -->
46
44
42
40
38
36
34
32
30
28
26
24
22
20
18
16
14
12
10
8
6
4
2
-0.3
-0.25
-0.2
-0.15
-0.1
-0.05
-1.4E-17
0.05
0.1
0.15
0.2
0.25

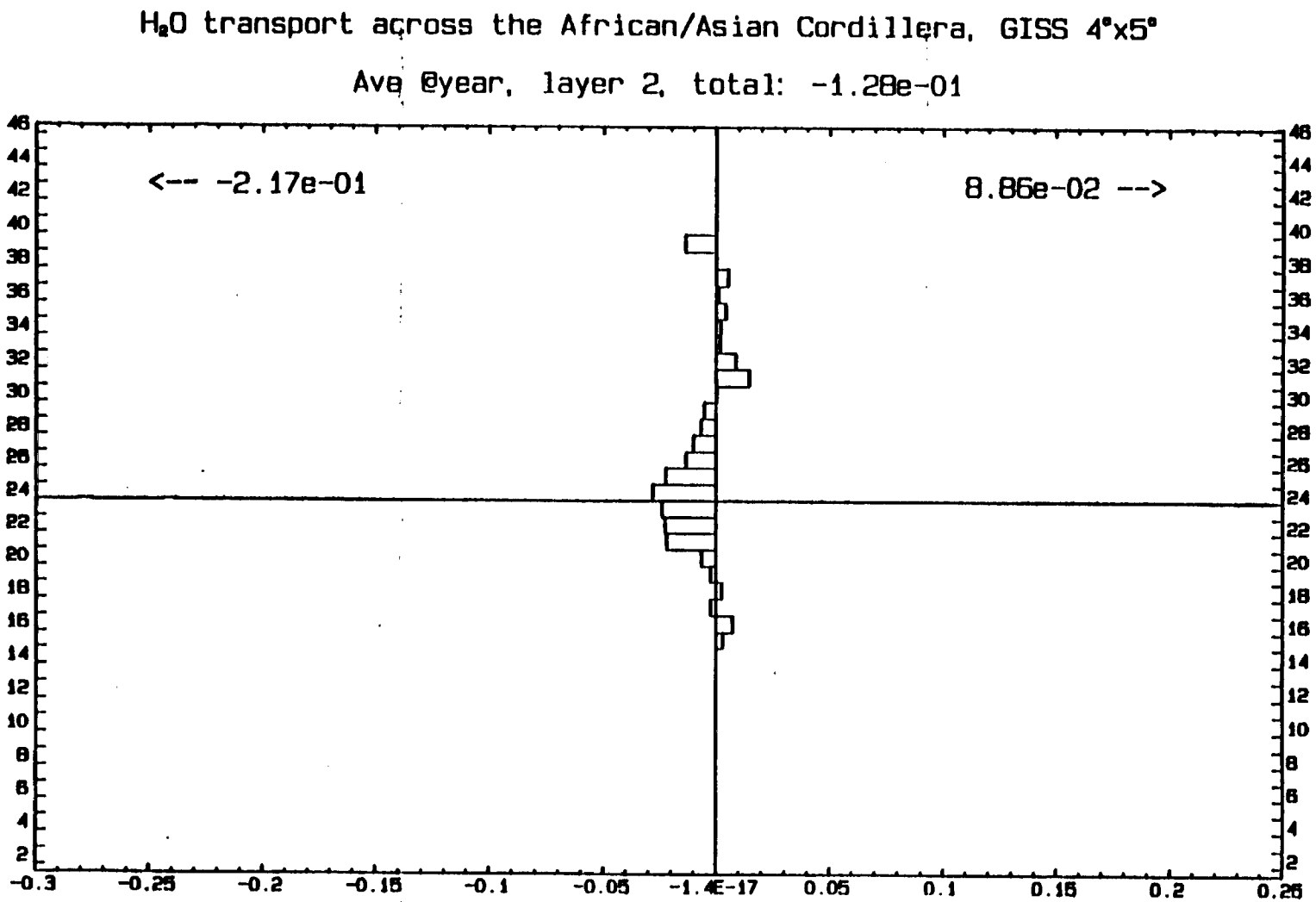
H2O transport across the African/Asian Cordillera, GISS 4°x5°
Ave @year, layer 2, total: -1.28e-01
<-- -2.17e-01
8.86e-02 -->
46
44
42
40
38
36
34
32
30
28
26
24
22
20
18
16
14
12
10
8
6
4
2
-0.3
-0.25
-0.2
-0.15
-0.1
-0.05
-1.4E-17
0.05
0.1
0.15
0.2
0.25

H_2O transport across the African/Asian Cordillera, GISS 4°x5°

Ave @year, layer 3, total: -6.82e-02

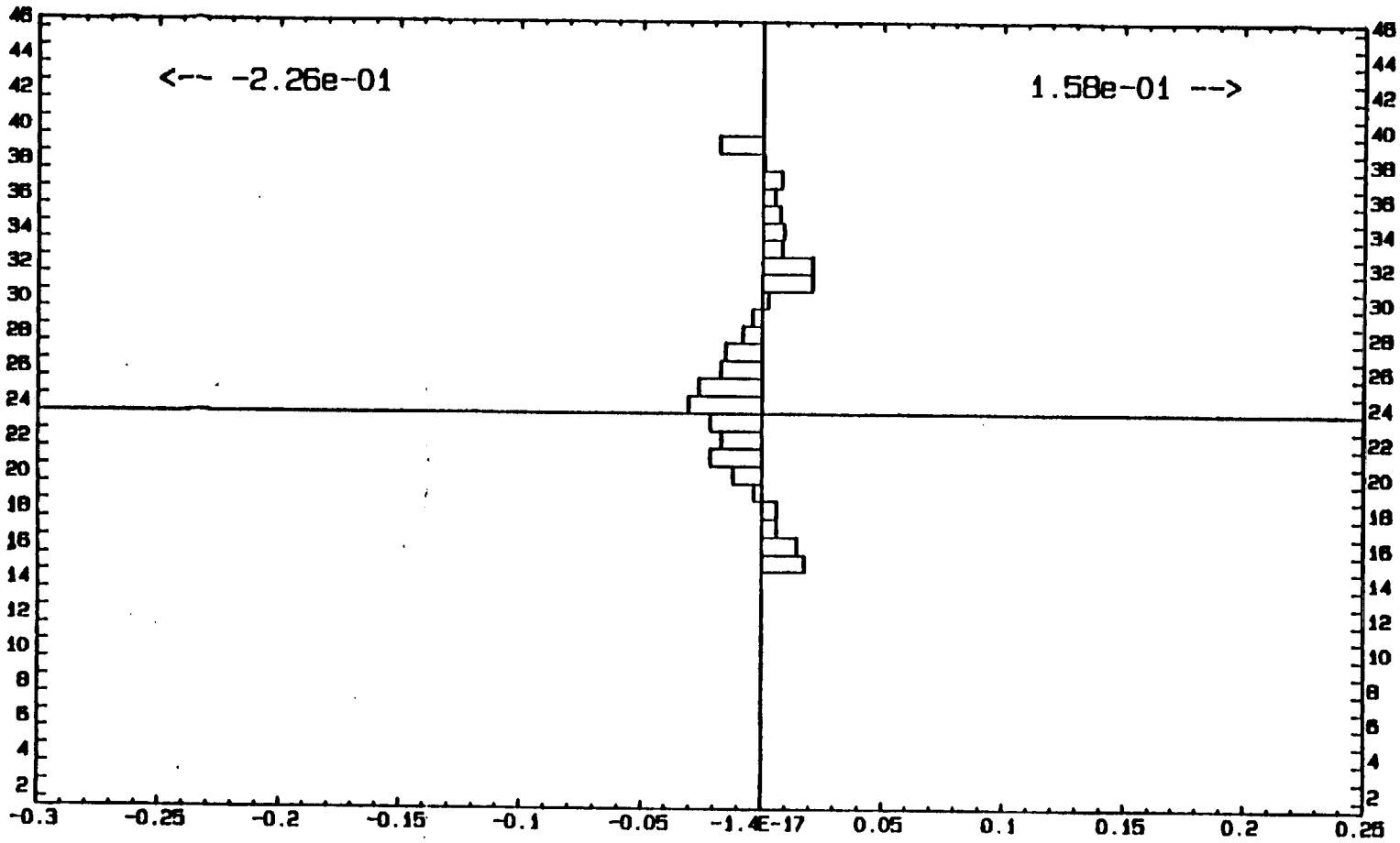

H_2O transport across the African/Asian Cordillera, GISS 4°x5°

Ave @year, layer 4, total: 3.26e-02

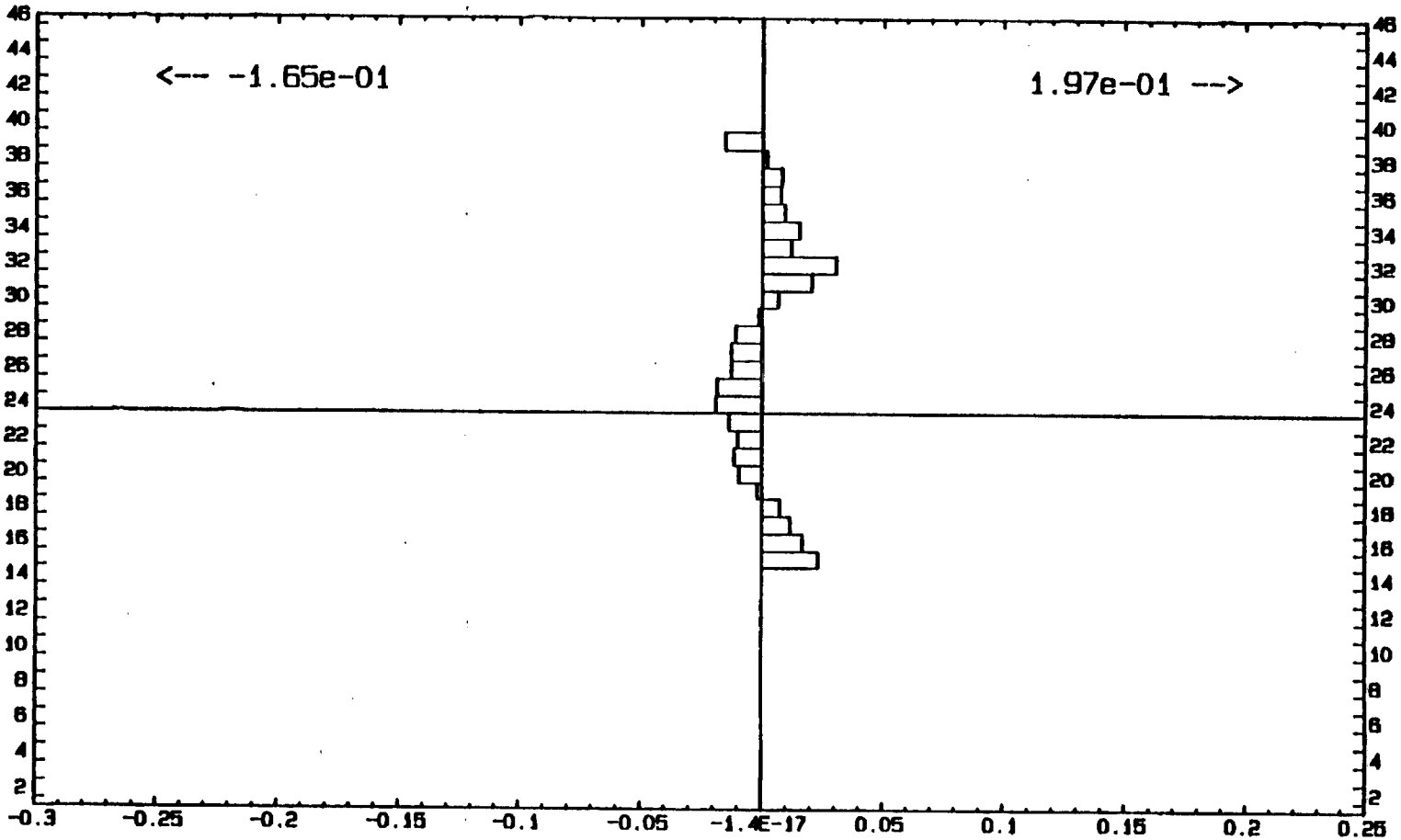

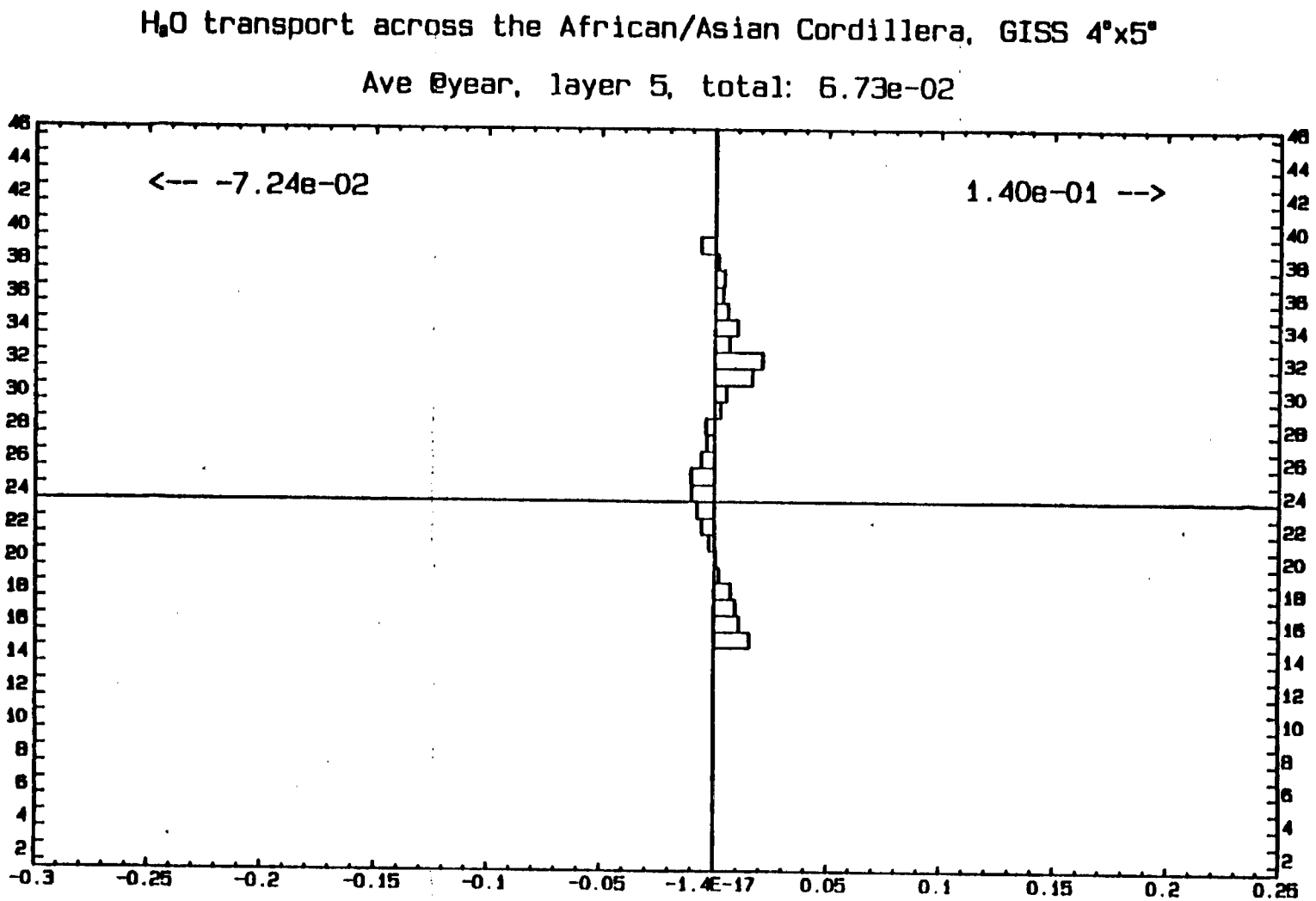
H₂O transport across the African/Asian Cordillera, GISS 4°x5°
Ave @year, layer 5, total: 6.73e-02
<-- -7.24e-02
1.40e-01 -->
46
44
42
40
38
36
34
32
30
28
26
24
22
20
18
16
14
12
10
8
6
4
2
-0.3
-0.25
-0.2
-0.15
-0.1
-0.05
-1.4E-17
0.05
0.1
0.15
0.2
0.25

Fig AM4 - AM10

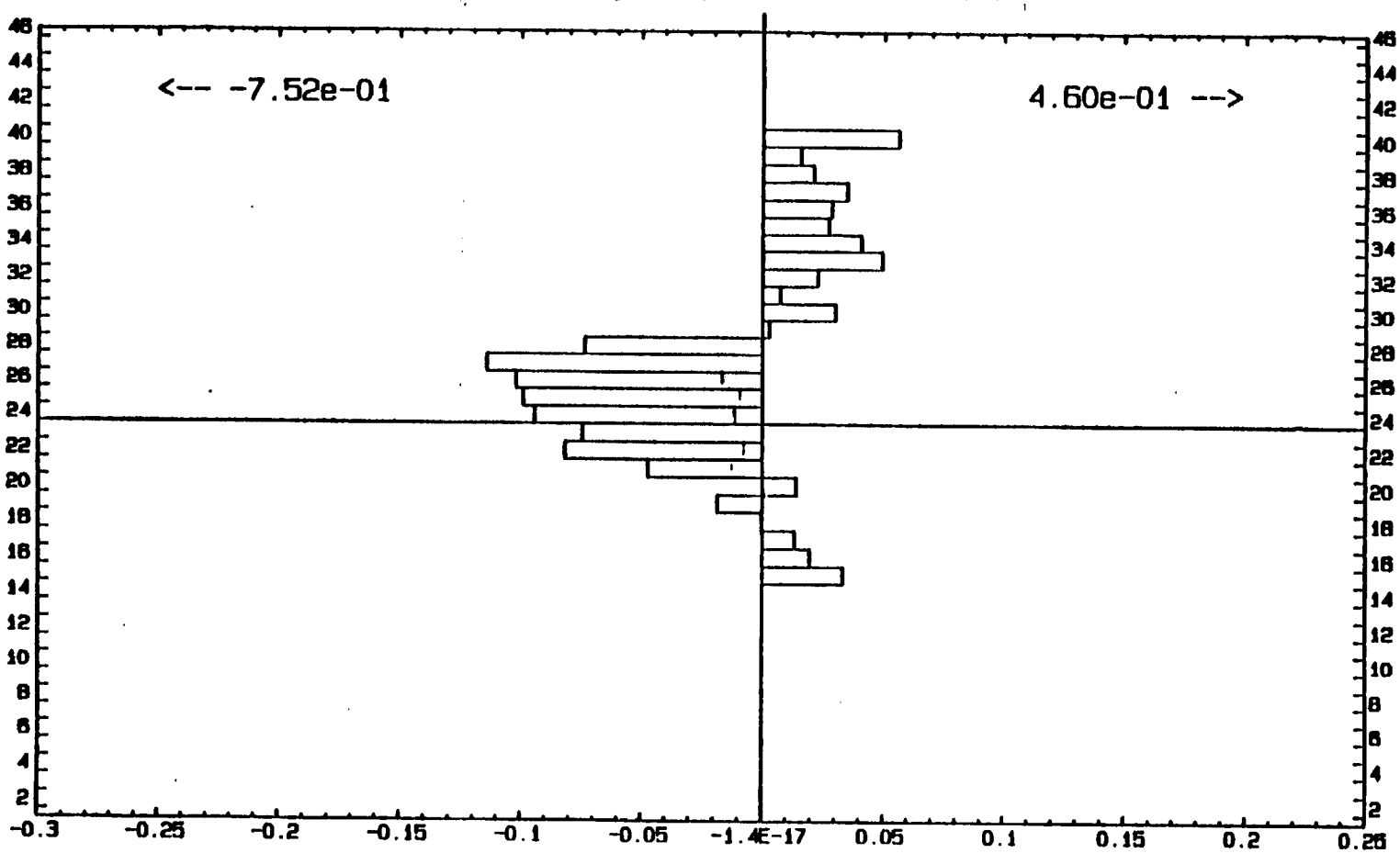
H₂O transport across the American Cordillera, GISS 4°x5°
Ave 0year, layer 0, total: -2.92e-01
<-- -7.52e-01
4.60e-01 -->
-0.3
-0.25
-0.2
-0.15
-0.1
-0.05
-1.4E-17
0.05
0.1
0.15
0.2
0.25

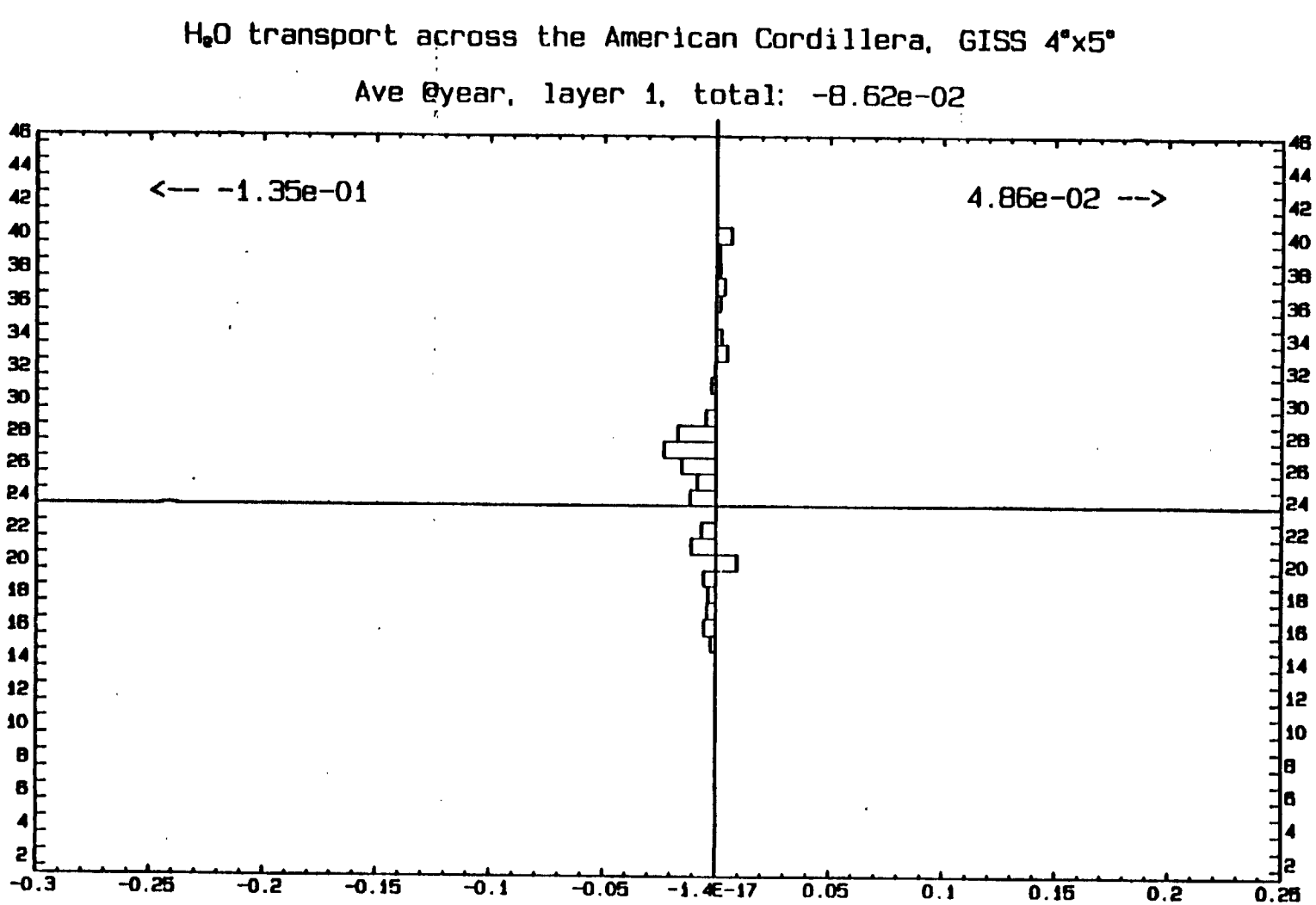
H2O transport across the American Cordillera, GISS 4°x5°
Ave @year, layer 1, total: -8.62e-02
<-- -1.35e-01
4.86e-02 -->
46
44
42
40
38
36
34
32
30
28
26
24
22
20
18
16
14
12
10
8
6
4
2
-0.3
-0.25
-0.2
-0.15
-0.1
-0.05
-1.4E-17
0.05
0.1
0.15
0.2
0.25

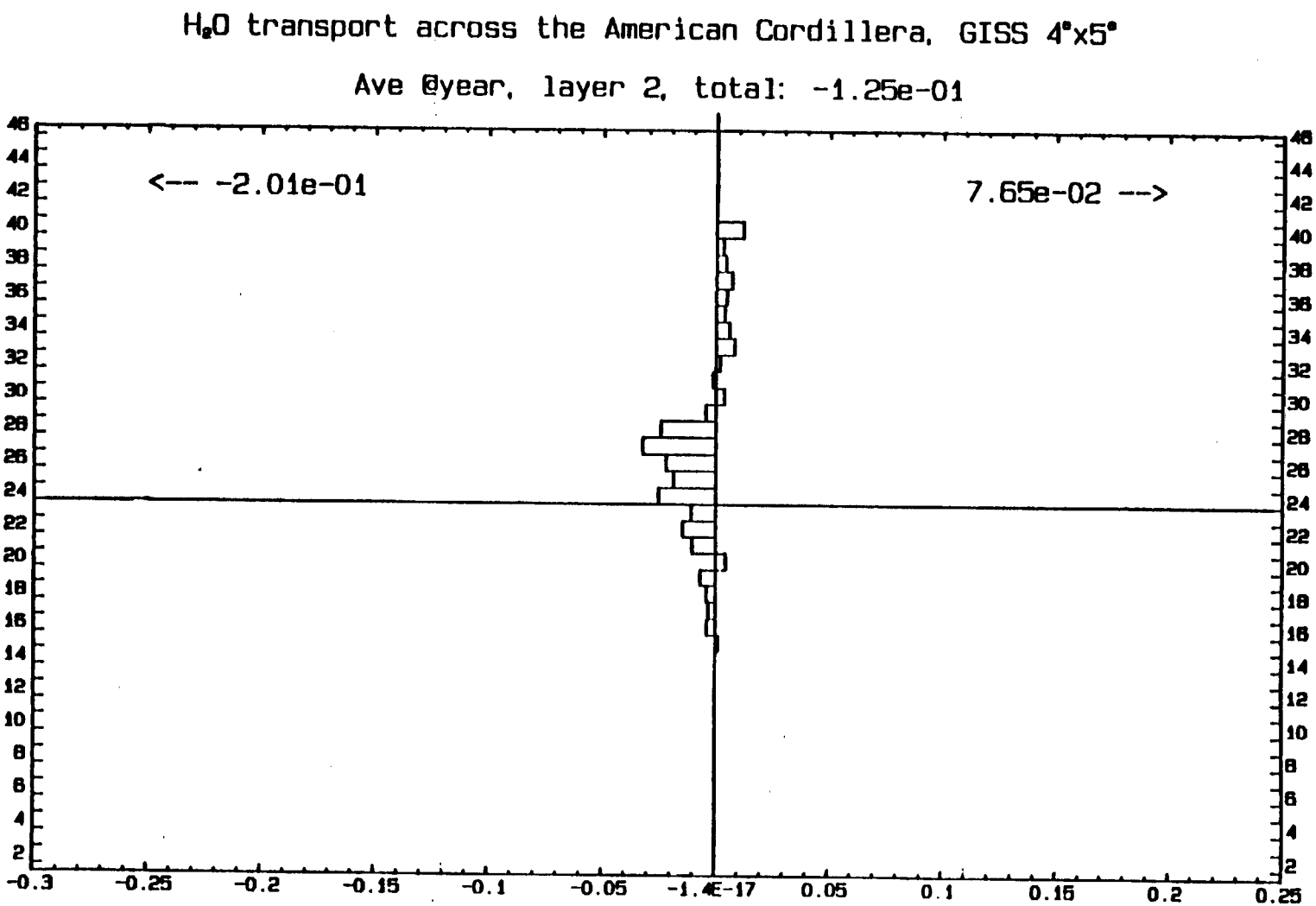
H_2O transport across the American Cordillera, GISS 4°x5°
Ave @year, layer 2, total: -1.25e-01
<-- -2.01e-01
7.65e-02 -->
46
44
42
40
38
36
34
32
30
28
26
24
22
20
18
16
14
12
10
8
6
4
2
-0.3
-0.25
-0.2
-0.15
-0.1
-0.05
-1.4E-17
0.05
0.1
0.15
0.2
0.25

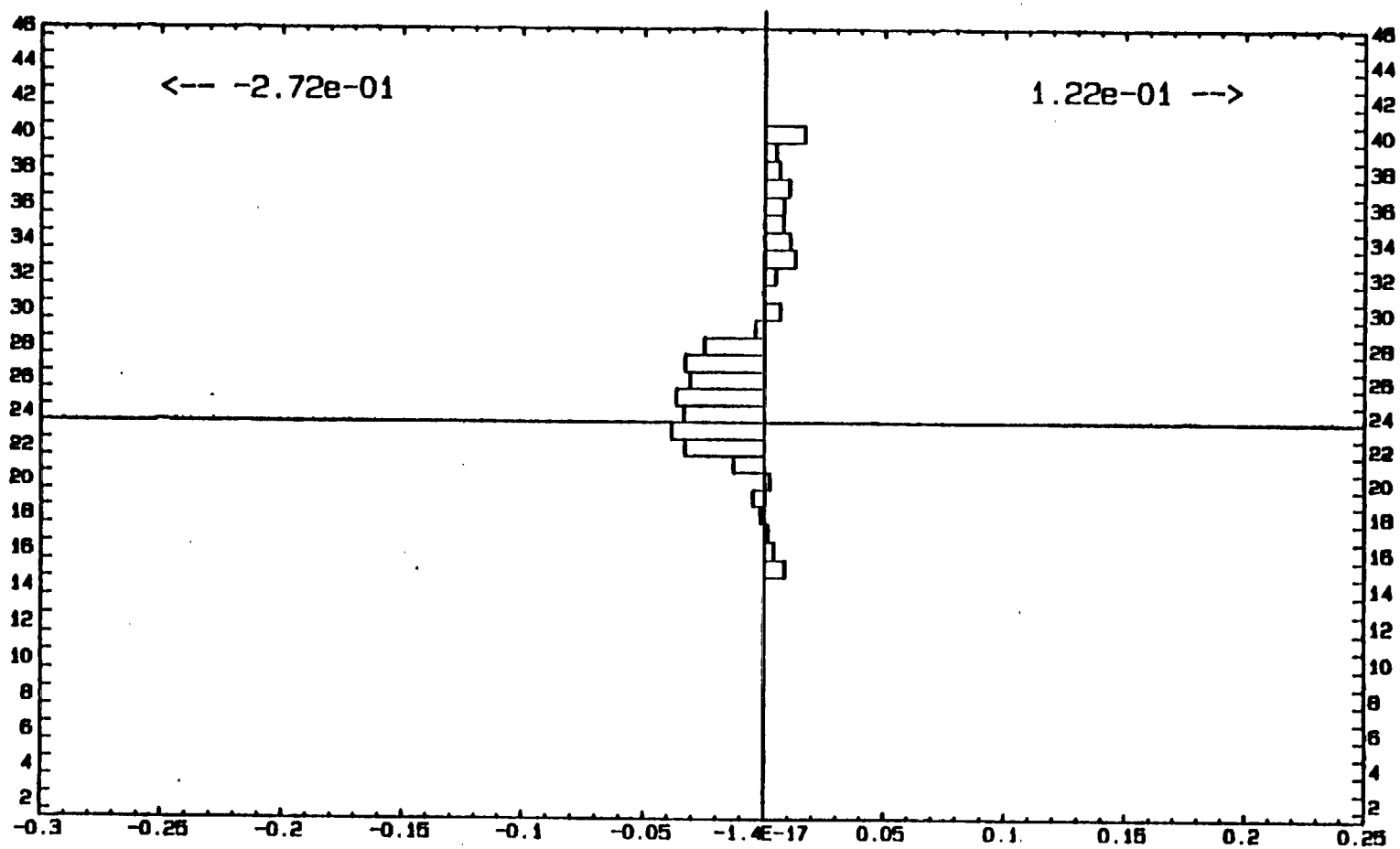
H₂O transport across the American Cordillera, GISS 4°x5°
Ave @year, layer 3, total: -1.49e-01
<-- -2.72e-01
1.22e-01 -->
46
44
42
40
38
36
34
32
30
28
26
24
22
20
18
16
14
12
10
8
6
4
2
-0.3
-0.25
-0.2
-0.15
-0.1
-0.05
-1.4E-17
0.05
0.1
0.15
0.2
0.25

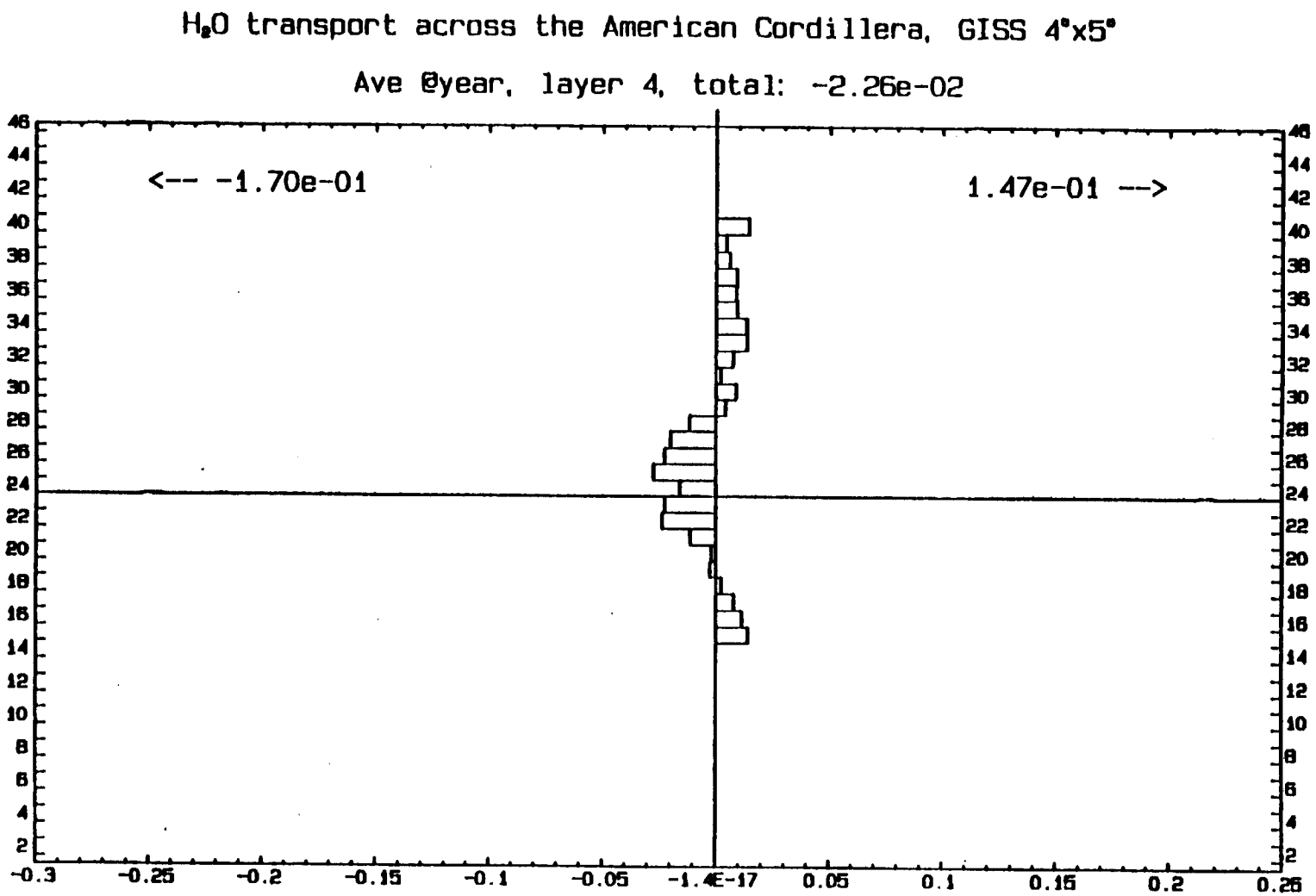
H2O transport across the American Cordillera, GISS 4°x5°
Ave @year, layer 4, total: -2.26e-02
<-- -1.70e-01
1.47e-01 -->
46
44
42
40
38
36
34
32
30
28
26
24
22
20
18
16
14
12
10
8
6
4
2
-0.3
-0.25
-0.2
-0.15
-0.1
-0.05
-1.4E-17
0.05
0.1
0.15
0.2
0.25

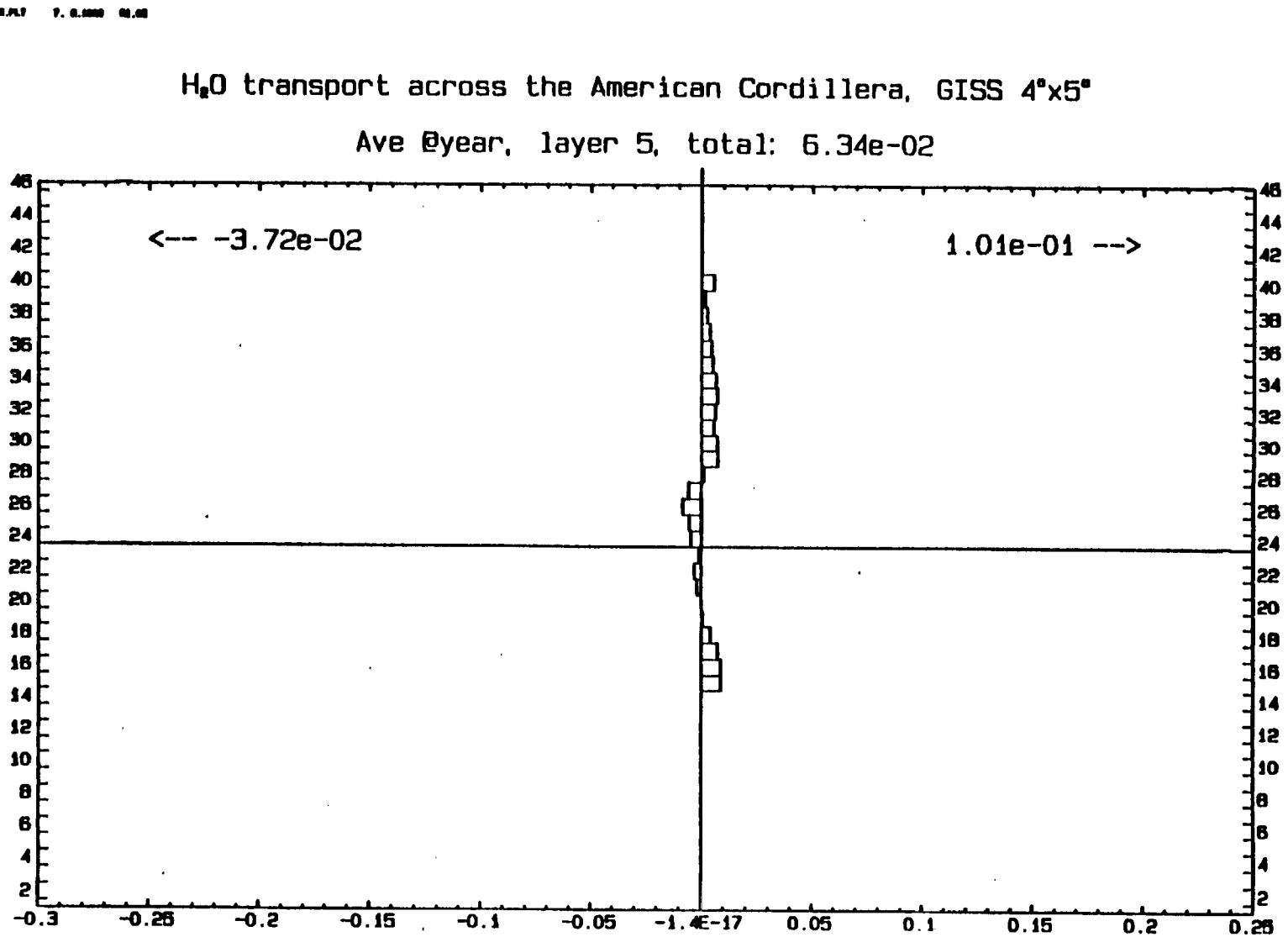
H2O transport across the American Cordillera, GISS 4°x5°
Ave @year, layer 5, total: 6.34e-02
<-- -3.72e-02
1.01e-01 -->
46
44
42
40
38
36
34
32
30
28
26
24
22
20
18
16
14
12
10
8
6
4
2
-0.3
-0.25
-0.2
-0.15
-0.1
-0.05
-1.4E-17
0.05
0.1
0.15
0.2
0.25

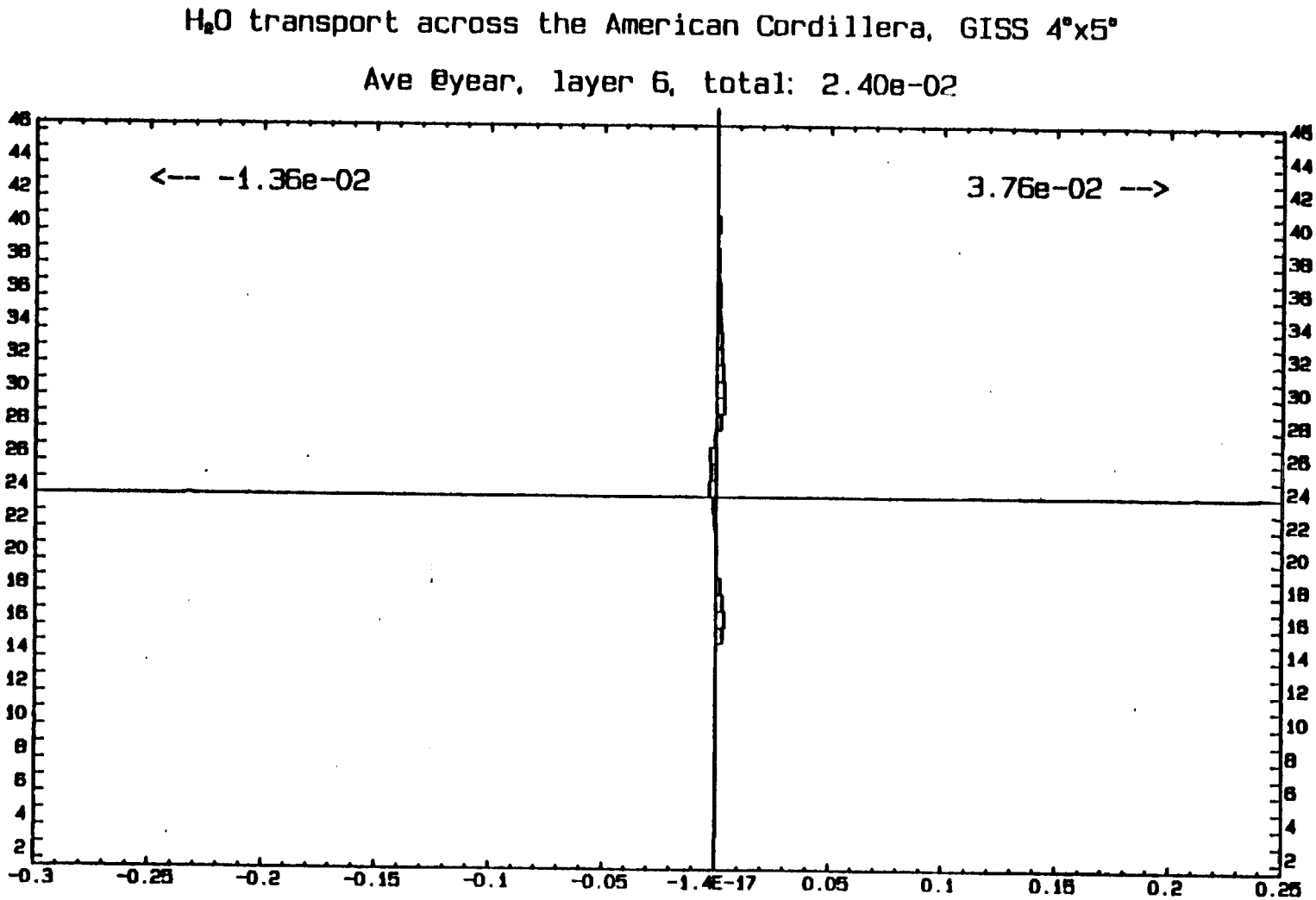
H_2O transport across the American Cordillera, GISS 4°x5°
Ave @year, layer 6, total: 2.40e-02
<-- -1.36e-02
3.76e-02 -->
46
44
42
40
38
36
34
32
30
28
26
24
22
20
18
16
14
12
10
8
6
4
2
-0.3
-0.25
-0.2
-0.15
-0.1
-0.05
-1.4E-17
0.05
0.1
0.15
0.2
0.25

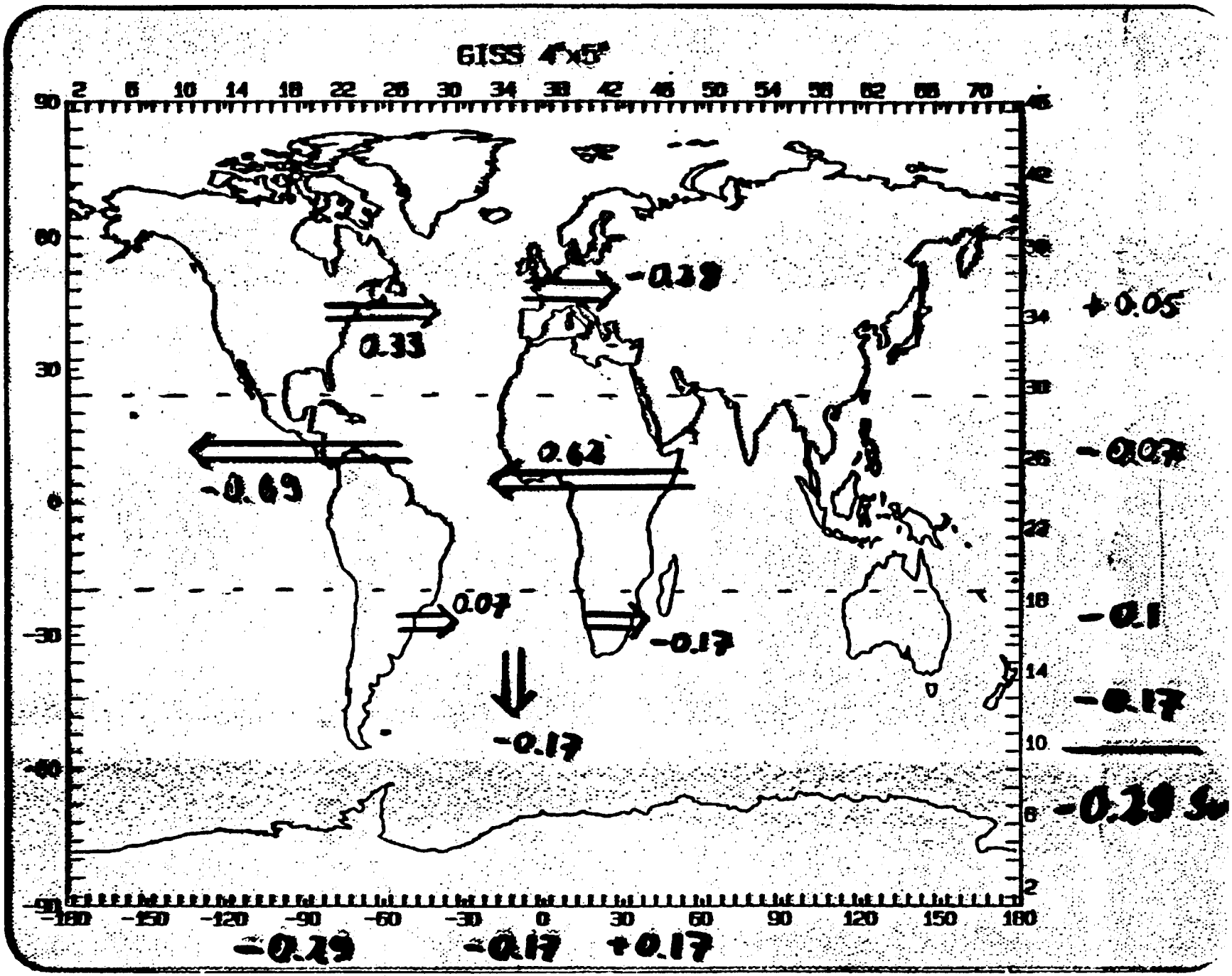

FRESH WATER BALANCE

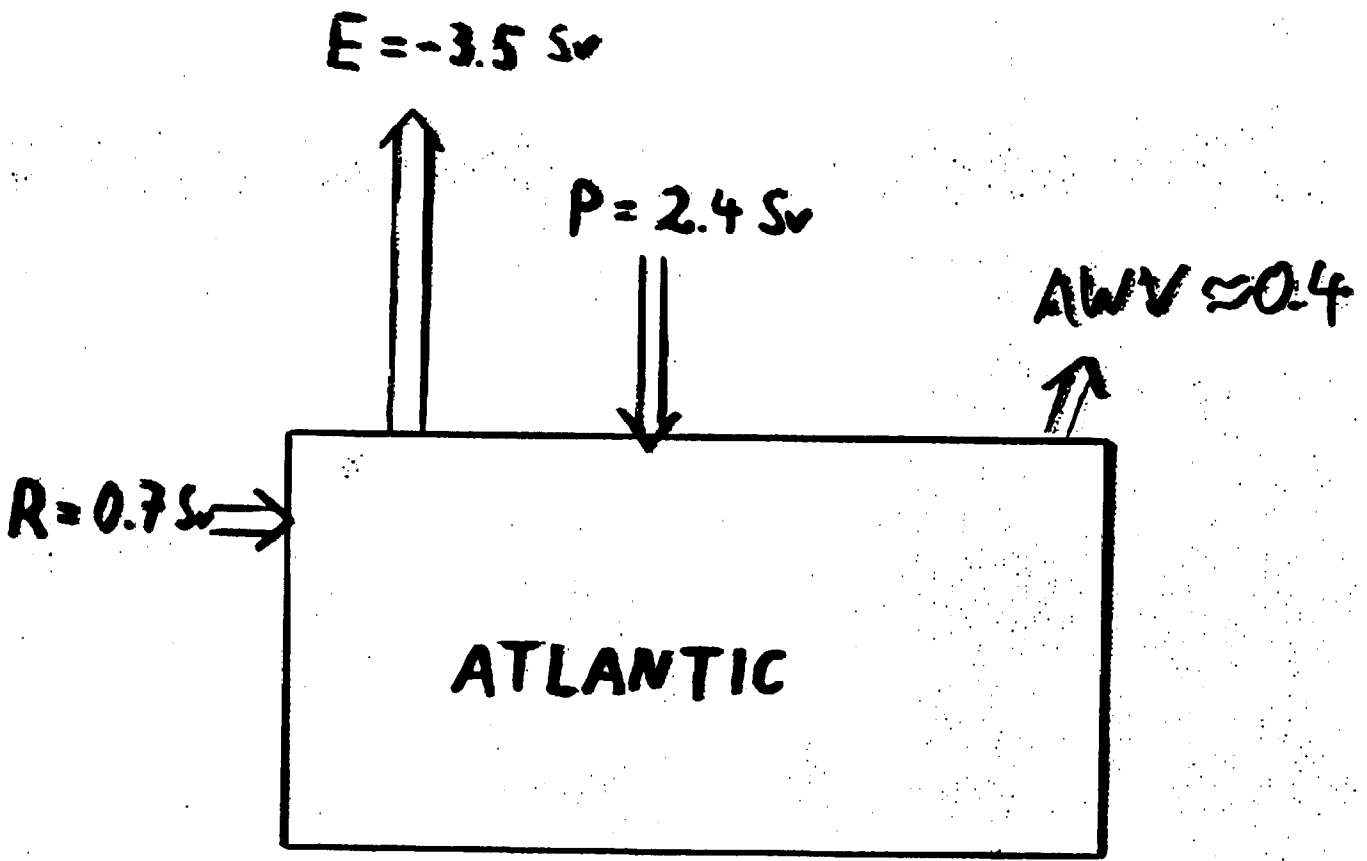

(BAUMGARTNER + REICHEL, 1975)

$1\,Sv = 10^6\ m^3/sec$

Polaroid

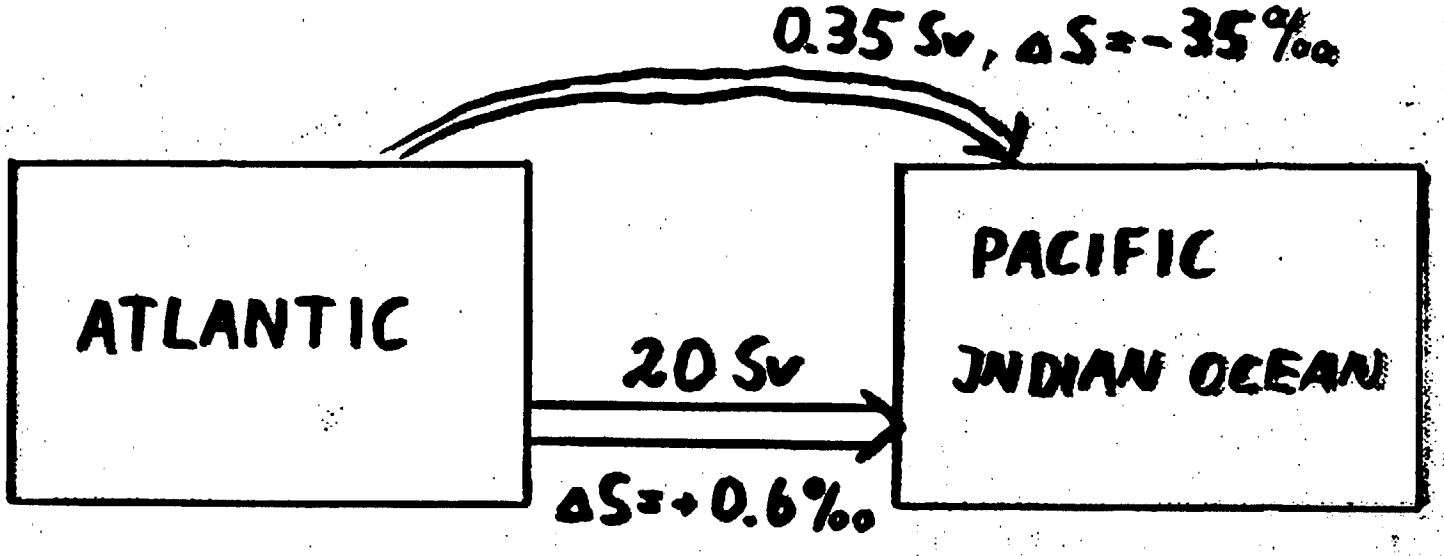

AMPLIFICATION: $\frac{NADW}{AWV} \approx 60$

APPENDIX II

Radon - 222

Radon was released into the 8° x 10° GCM uniformly from all non ice covered areas of the continents. Runs were made for 12 months. The model was preconditioned for one month so as to start the run with the radon distribution at approximate steady state.

Shown in figure 1 are the geographic distributions of radon for the months of July and January.

Shown in figures 2 and 3 are zonal sections of radon versus height at ≈44°S and at ≈44°N for July and for January. Shown in figures 4 and 5 are meridional sections at ≈20°E and at ≈90°W.

Lead 210

Lead 210 is produced by the decay of radon. The mean annual vertically integrated production function is shown in figure 6. The lead atoms are assumed to be removed from the air entirely by precipitation. Two extreme assumptions are used. In one case lead atoms are assumed to follow water molecules as if they were isotopes of water. The fallout pattern produced using this assumption is shown in figure 7a. The other extreme is to assume that all the lead atoms available are incorporated in precipitation that forms and once in precipitation, none evaporate. The fallout pattern produced in this way is shown in figure 7b.

Shown in figure 8 are the annual average lead -210 concentration pattern for the models lowest layer for $\propto = 1$ and for $\propto = \infty$.

Figure 1. Average radon concentration in arbitrary units in the lower layer of the GISS 8° x 10° grid model for the months of June, July and August (1a) and for the months December, January and February (1b).

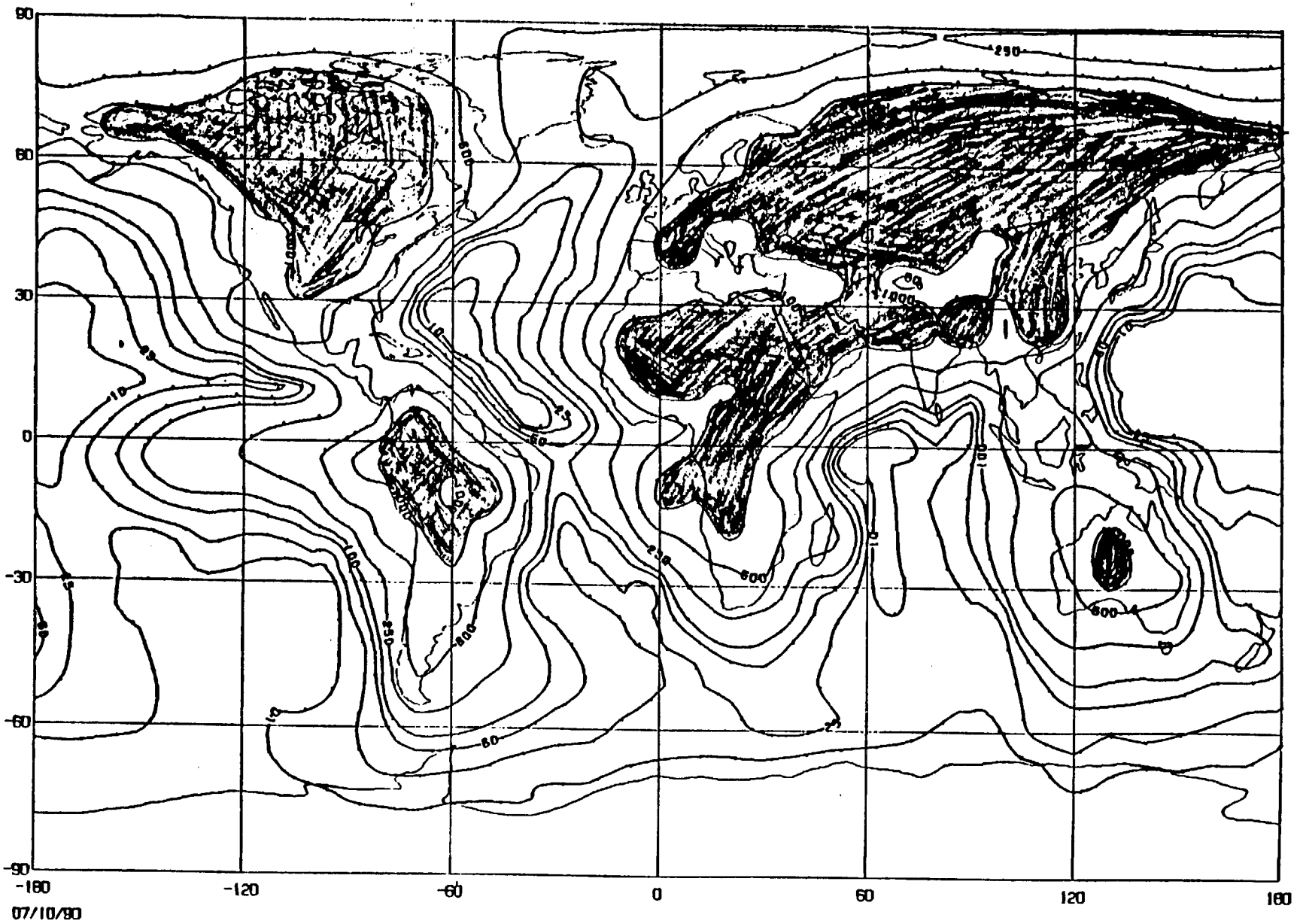

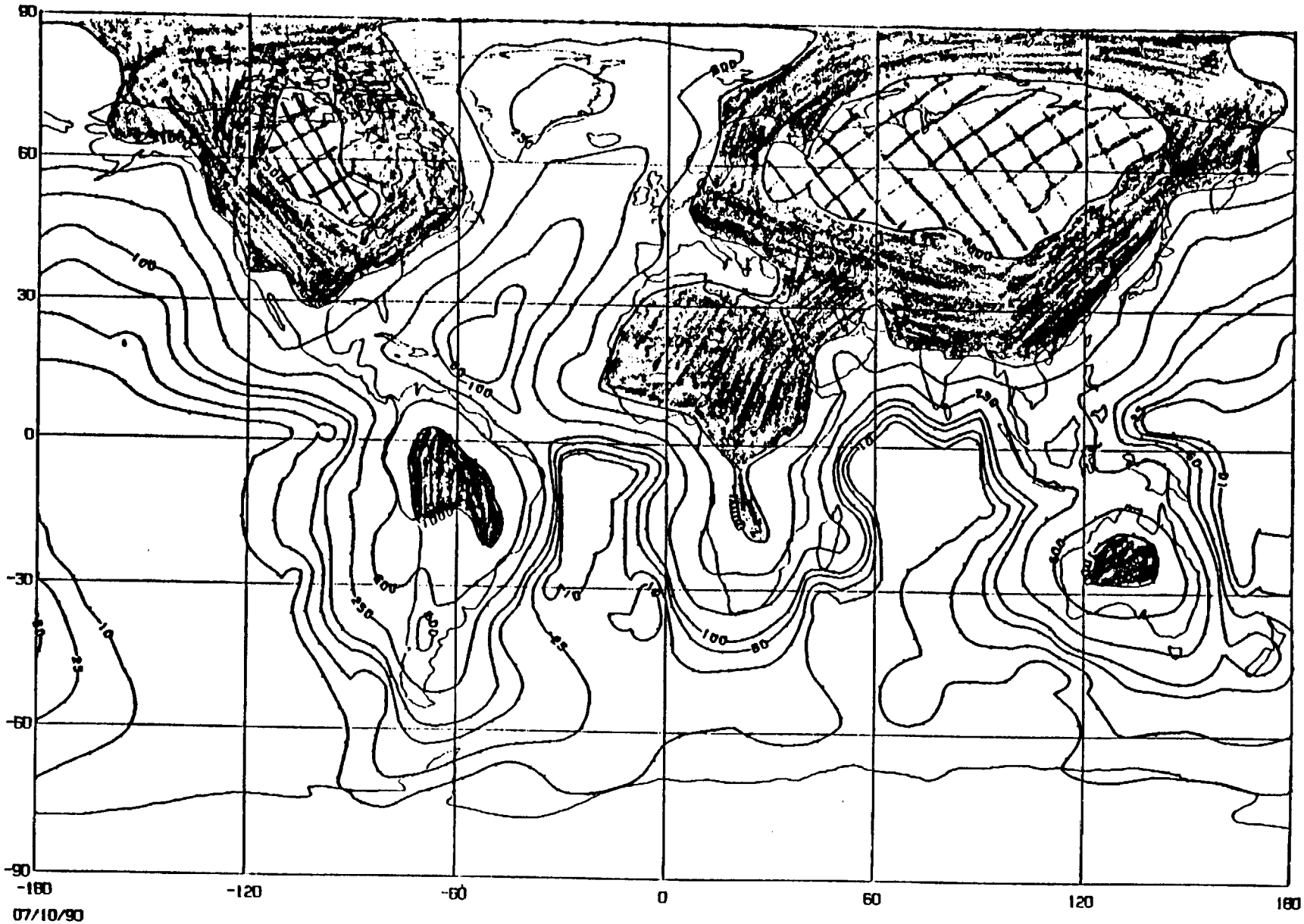
90
60
30
0
-30
-60
-90
-180
-120
-60
0
60
120
180
07/10/90

Figure 2. Vertical section of atmospheric radon concentration drawn along 44°S for June, July and August (2a) and for December, January and February (2b).

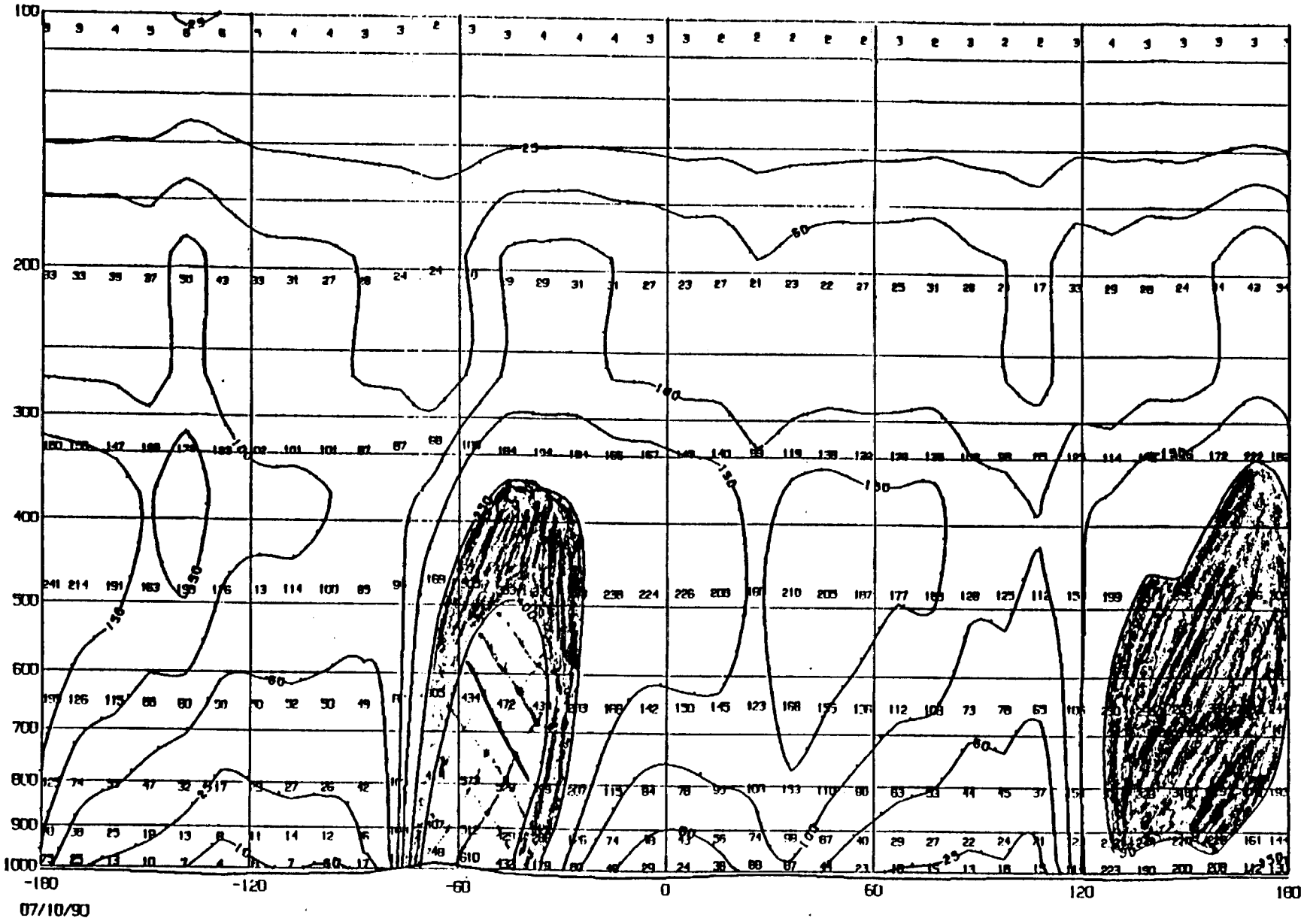

448

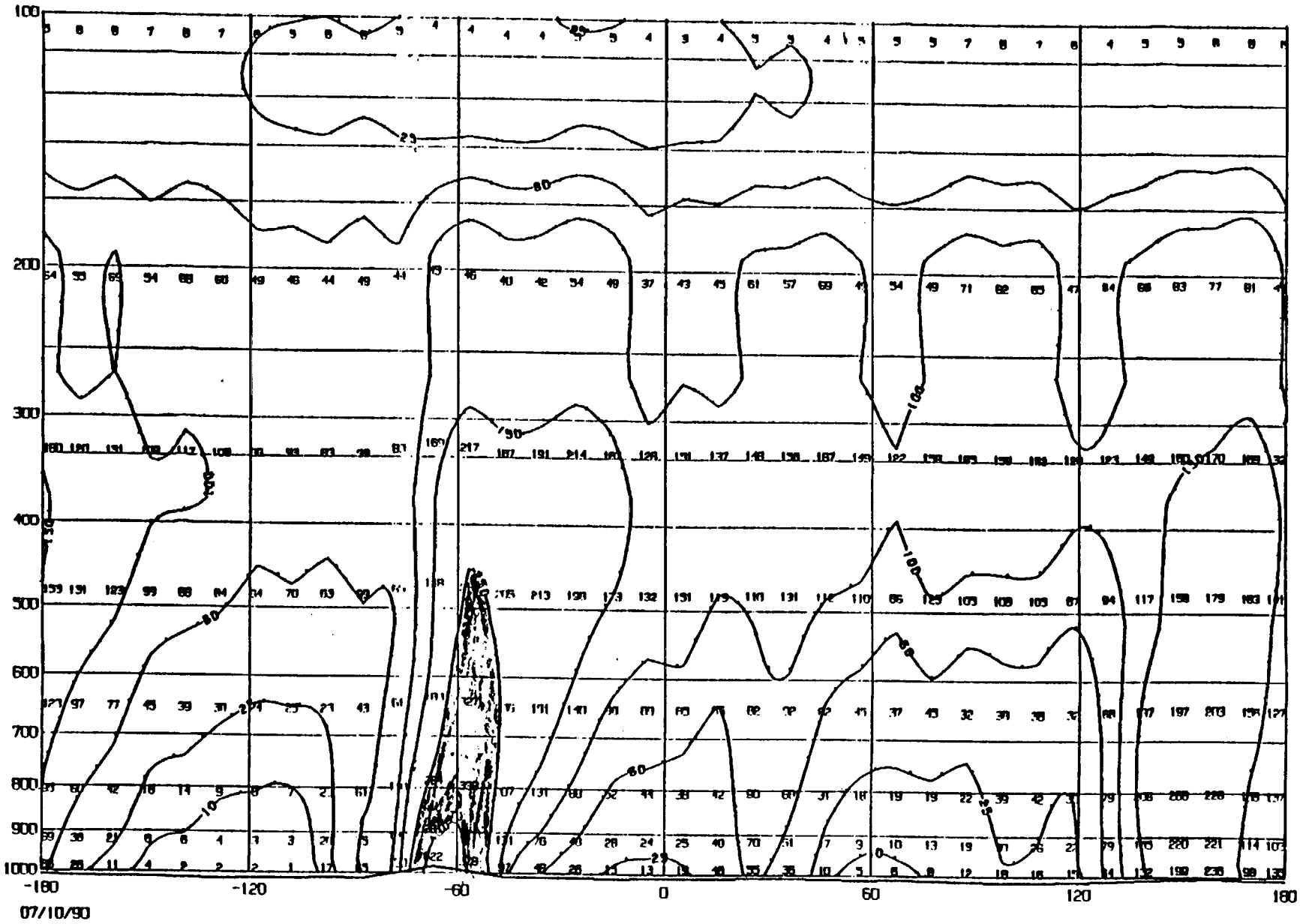

Figure 3. Vertical section of atmospheric radon concentration drawn along 44°N for June, July and August (3a) and for December, January and February (3b).

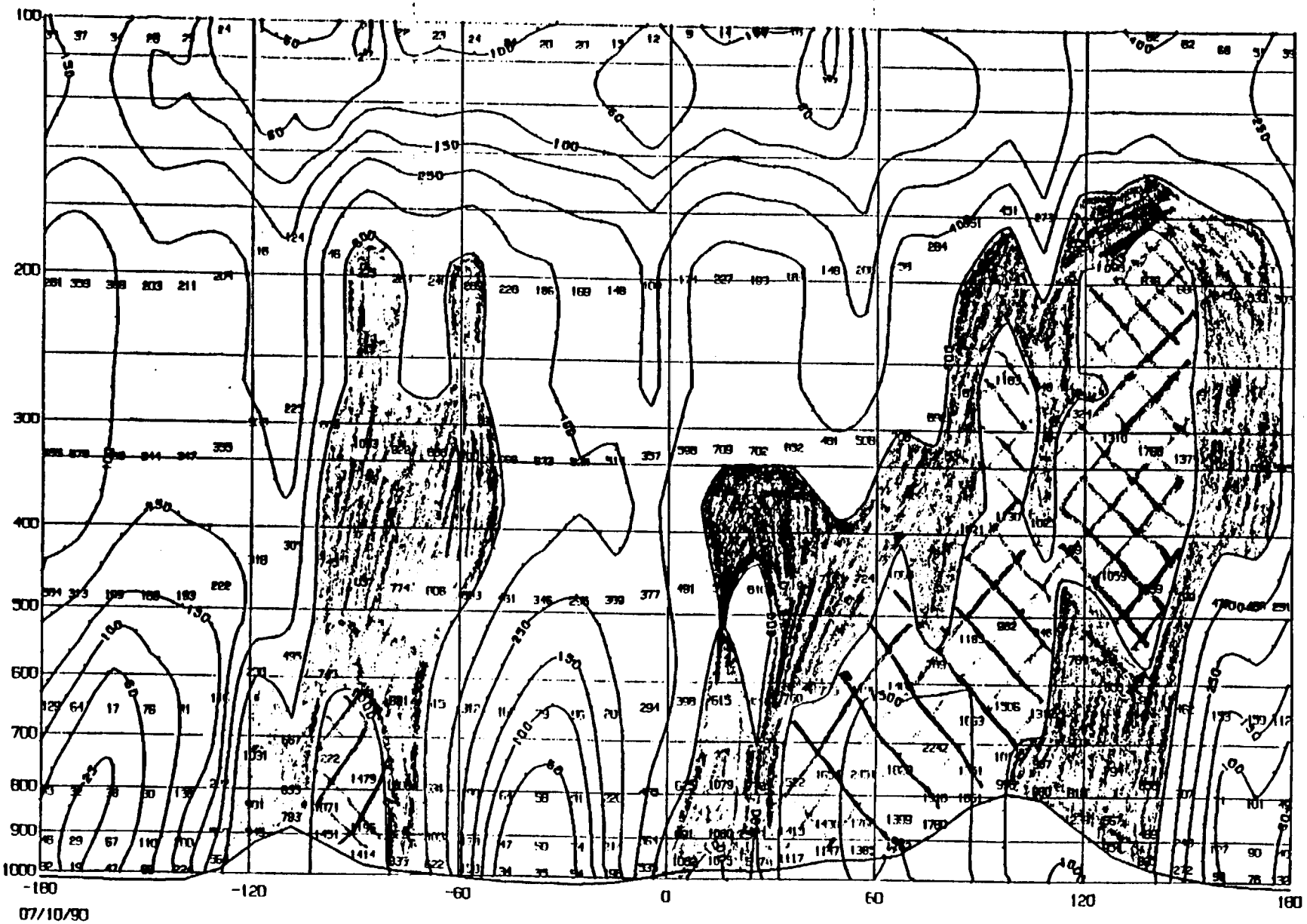

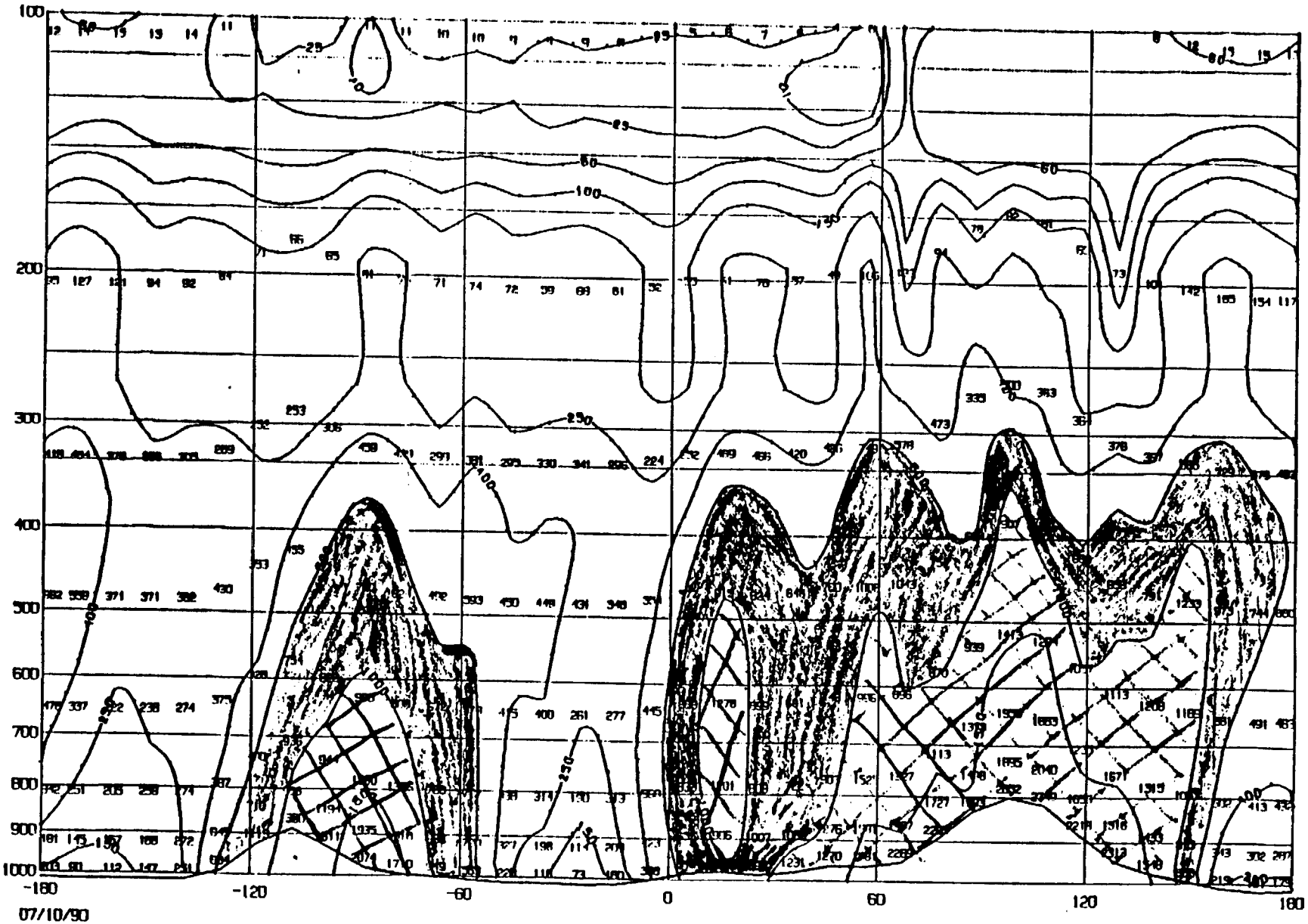

ORIGINAL PAGE IS
OF POOR QUALITY

Figure 4. Vertical section of atmosphere radon drawn along ~90°W meridian for June, July and August (4a) and for December, January and February (4b).

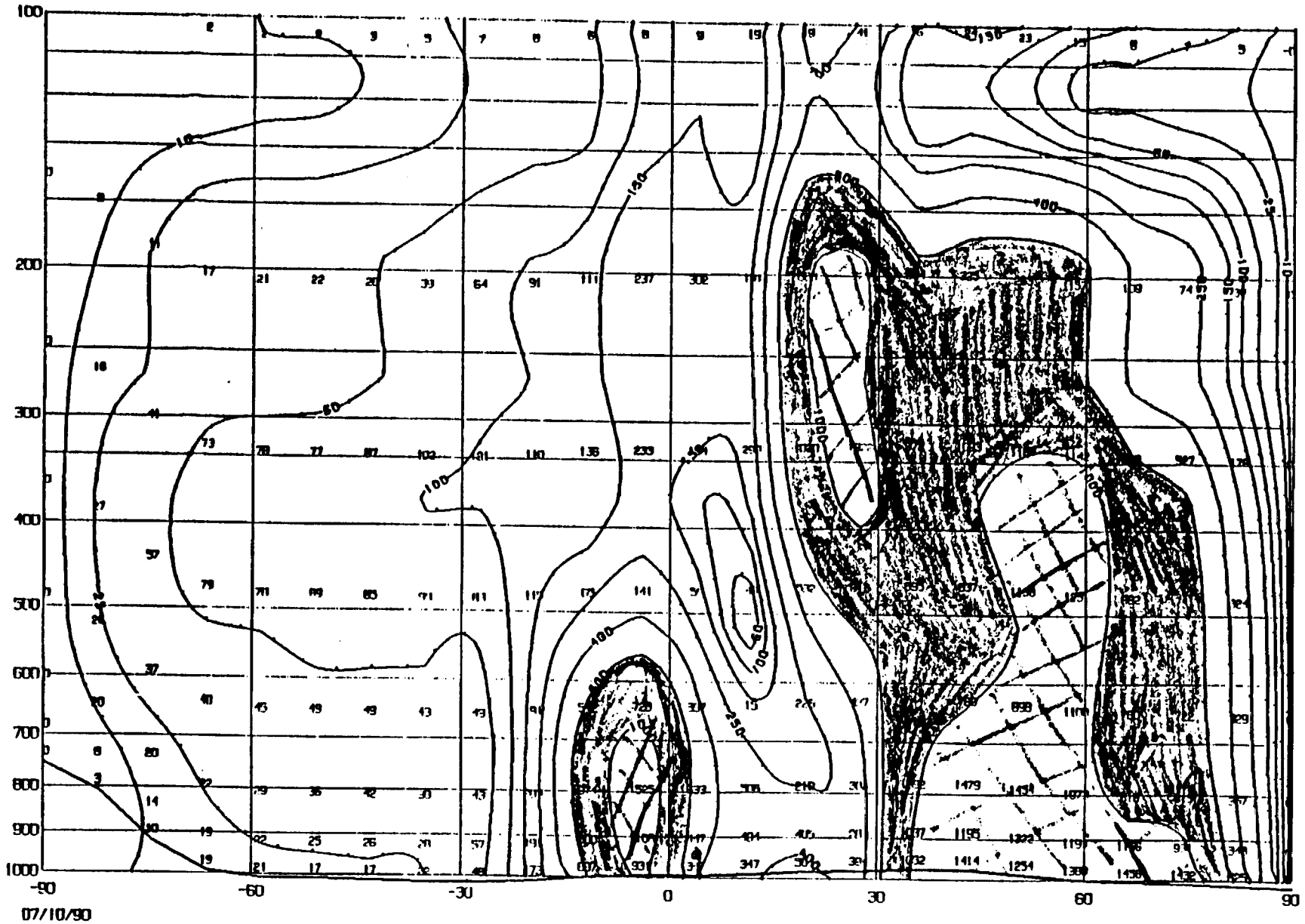

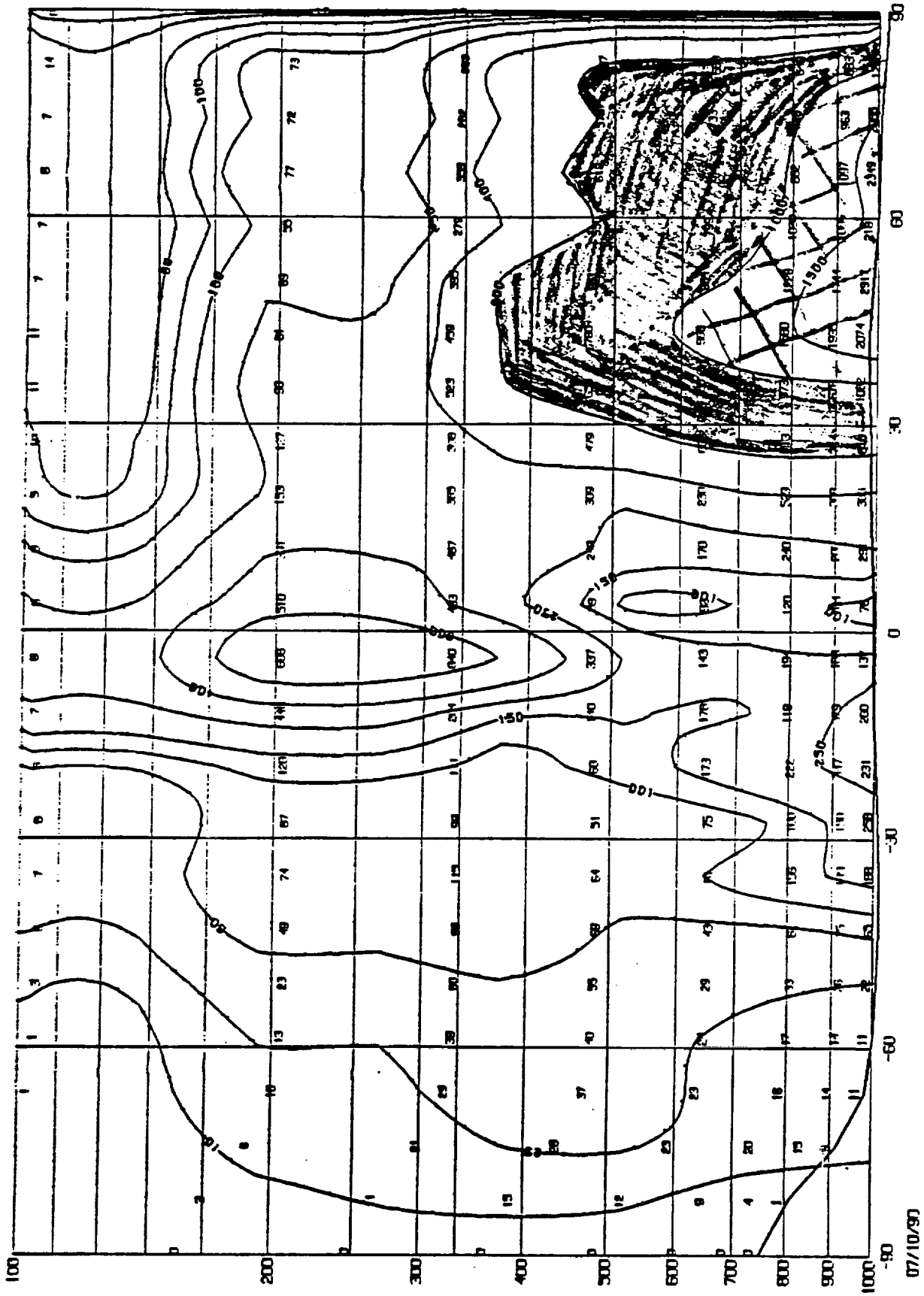

ORIGINAL PAGE IS
OF POOR QUALITY

Figure 5. Vertical section of radon drawn along the ≈20°E meridian for June, July and August (5a) and for December, January and February (5b).

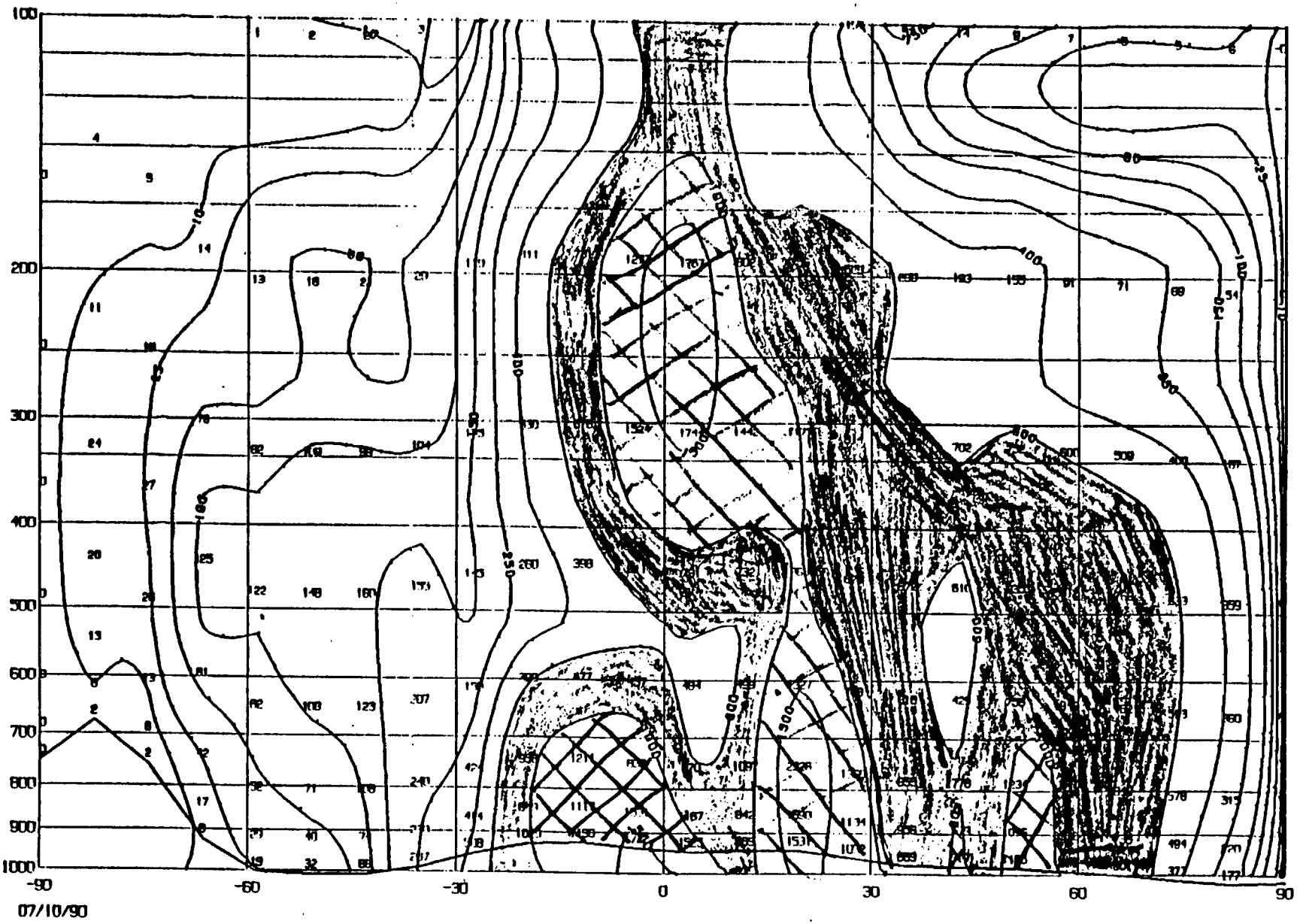

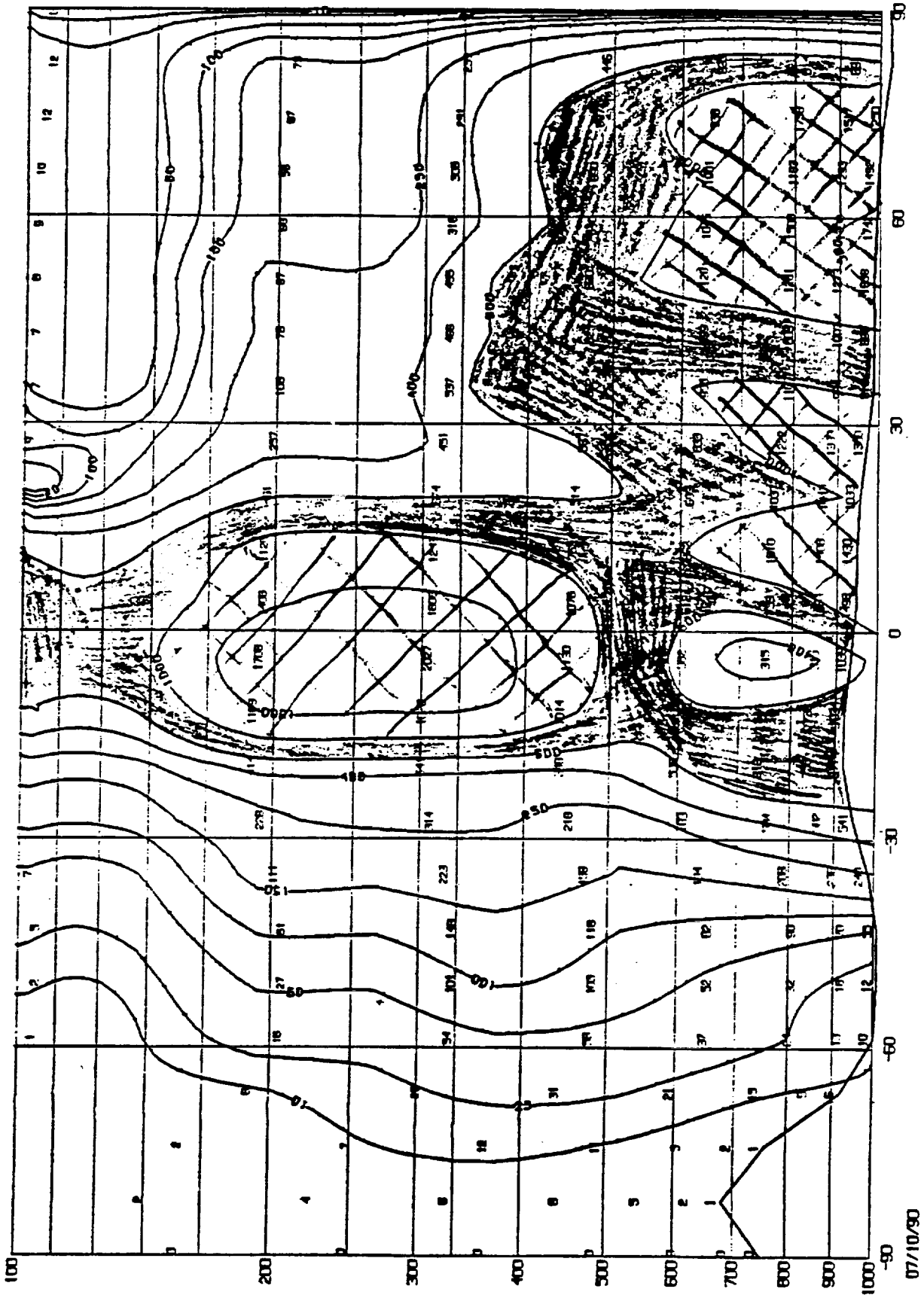

ORIGINAL PAGE IS
OF POOR QUALITY

Figure 6. Decay rate of radon integrated over the air column and averaged over the whole year. This is the ^{210}Pb source function.

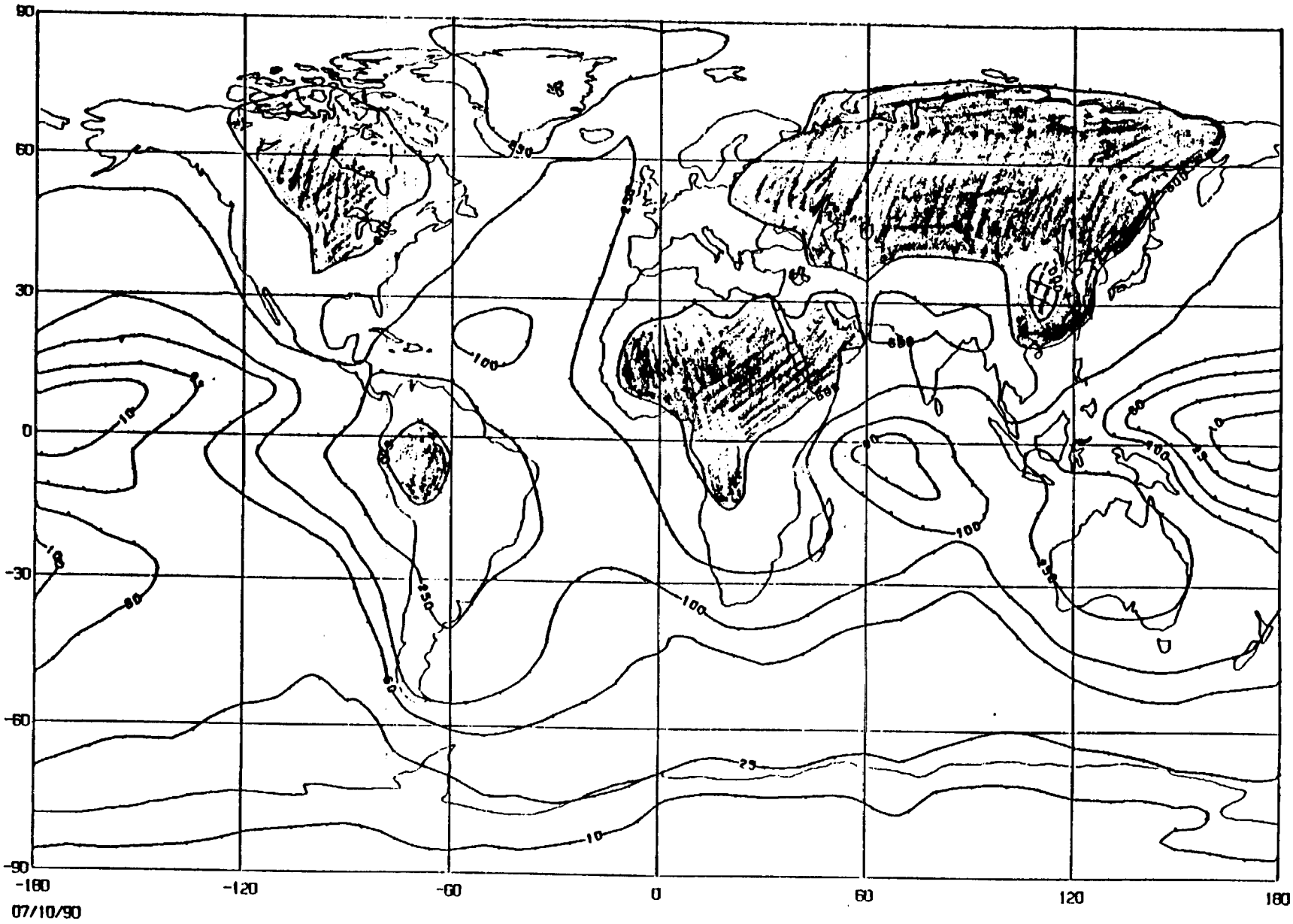

Figure 7. ^{210}Pb rainout patterns (averaged over an entire year) for two limiting case assumptions with regard to removal kinetics. In the first (7a), ^{210}Pb atoms are treated as isotopes of water. The same fraction of ^{210}Pb and water condense to form precipitation (and if evaporation occurs the same fraction evaporate) We call this the $\alpha = 1$ case. In the second (7b) all the ^{210}Pb atoms go to the precipitation and none evaporates. We call this the $\alpha = \infty$ case.

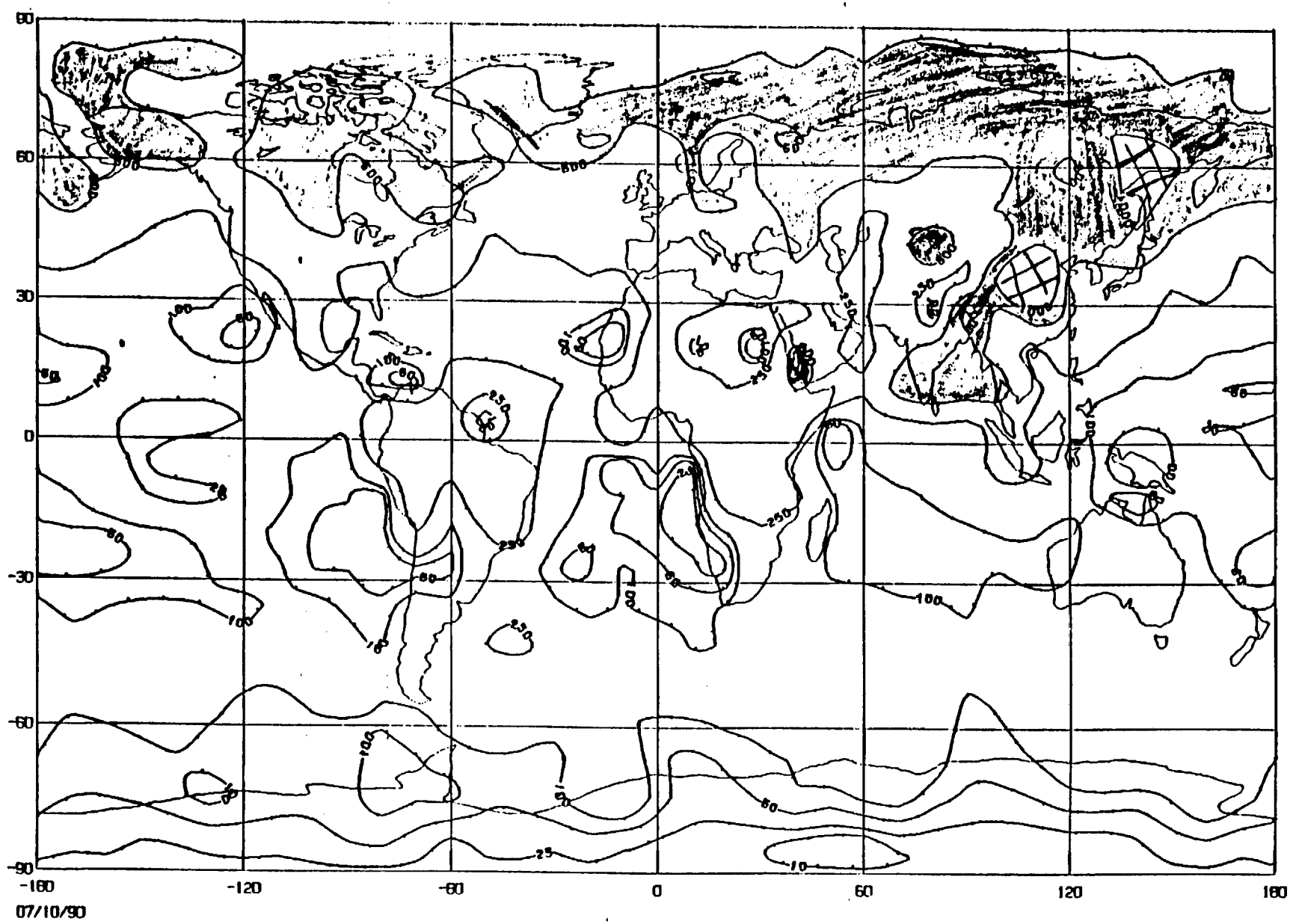

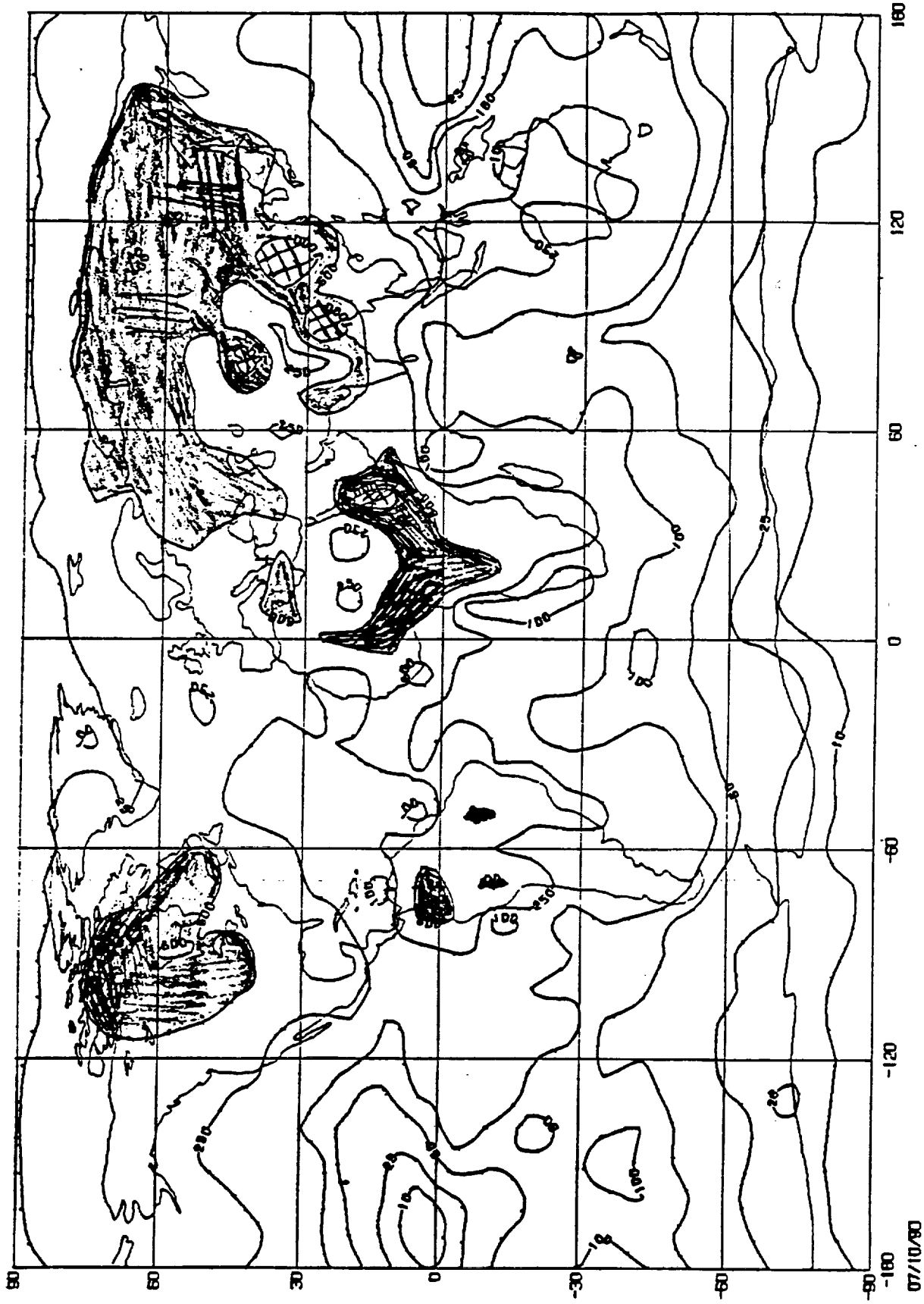

Figure 8. Mean annual ^{210}Pb concentrations in ground layer air for the Pb concentrations in ground layer air for the $\alpha = 1$ case (8a) and for the $\alpha = \infty$ case (8b).